Atmospheric Research 264 (2021) 105824

Contents lists available at ScienceDirect

Atmospheric Research

journal homepage: www.elsevier.com/locate/atmosres

Sensitivity of near-surface meteorology to PBL schemes in WRF simulations in a port-industrial area with complex terrain

Serena Falasca [a,b], Ilaria Gandolfi [a,b,*], Stefania Argentini [c], Francesca Barnaba [c], Giampietro Casasanta [c], Luca Di Liberto [c], Igor Petenko [c], Gabriele Curci [a,b]

[a] Department of Physical and Chemical Sciences, University of L'Aquila, 67100, L'Aquila, Italy
[b] Center of Excellence for the Remote Sensing and Forecast of Severe Weather (CETEMPS), Department of Physical and Chemical Sciences, University of L'Aquila, 67100, L'Aquila, Italy
[c] National Research Council, Institute of Atmospheric Sciences and Climate, ISAC-CNR, Via Fosso del Cavaliere, 100, 00133 Rome, Italy

ARTICLE INFO

Keywords:
WRF
PBL schemes
BEP
Coast
Wind
Temperature

ABSTRACT

Parameterizations of the Planetary Boundary Layer (PBL) embedded in numerical weather prediction models are crucial in the simulation of local meteorology and require a special investigation. In this study we evaluate simulations at 1 km horizontal resolution using six PBL schemes of the Weather Research and Forecasting model (WRF) by comparison to observations performed in a coastal port-industrial area (Civitavecchia) on the Tyrrhenian coast of Central Italy. During the measurement campaign (April 2016) three types of atmospheric circulation regimes were identified: "breeze", "jet" and "synoptic". Some generalizations can be inferred from the results, despite the variety of settings analyzed (two sites, three regimes in both day and night conditions). Our results show that the temperature simulation is much more sensitive to the configuration at night than during the day, especially on breeze days, when the occurrence of stable boundary layer is favored. For wind speed, non-local schemes are very similar to each other, unlike the local closure schemes.

The use of the urban Building Environment Parameterization (BEP) significantly improves the simulation of the 2 m temperature during the "jet" evenings and nights, while it entails a further overestimation of the temperature during the "breeze" days leading to a reduction of the bias.

1. Introduction

Numerical weather prediction is now widely applied in different scientific fields besides weather forecasting, for example as driver for air quality simulation or in 'what-if' scenarios at different spatial and temporal scales. In such models, based on a set of equations describing the flow of fluids, a physical process that cannot be directly defined requires a parameterization based on reasonable physical or statistical representations (NOAA). A parameterization is "an approximation to nature" (Stull, 1988) and many have been developed over time. Parameterization options embedded in numerical weather prediction models usually concern planetary boundary layer (PBL), land and urban surface, surface layer, cloud microphysics, and radiation.

Several parameterizations are available in the state of the art Weather Research and Forecasting model (WRF). Many studies investigated the sensitivity of the model results to these, and particularly in relation to microphysics and cumulus (e.g., Karki et al., 2018; Hasan and Islam, 2018; Reshmi Mohan et al., 2018; Jeworrek et al., 2019), radiation (e.g., Zempila et al., 2016; Sun and Bi, 2019), land surface (e.g., Zeng et al., 2015; Tomasi et al., 2017; Zhang et al., 2020), or a combination of the previous ones (e.g., Gunwani et al., 2020). The PBL schemes have been specially evaluated because of their crucial role in the representation of land and ocean – atmosphere exchanges of mass, energy, moisture, and therefore in the simulation results (Chaouch et al., 2017). Several studies on the intercomparisons of PBL schemes in WRF have also been published (e.g., Gunwani and Mohan, 2017; Sathyanadh et al., 2017). A summary of these is reported in Table 1. Findings are highly specific to each application, and an overall evaluation of the skills of the different PBL schemes is difficult (Xu et al., 2019), nevertheless some remarks recur. As found by Banks and Baldasano (2016) and Avolio et al. (2017), the Assymetric Convective Model Version 2 (ACM2) and Yonsei University (YSU) schemes have a better model-observations agreement for wind speed and PBL height (PBLH), whereas their outcomes differ in skills in terms of temperature simulation: it is better for Bougeault-Lacarrère (BL) according to Banks and Baldasano (2016),

* Corresponding author at: Department of Physical and Chemical Sciences, University of L'Aquila, 67100 L'Aquila, Italy.
E-mail address: ilaria.gandolfi@aquila.infn.it (I. Gandolfi).

https://doi.org/10.1016/j.atmosres.2021.105824
Received 26 May 2021; Received in revised form 11 August 2021; Accepted 23 August 2021
Available online 25 August 2021
0169-8095/

Nomenclature

ACM2	Asymmetric Convection Model 2 scheme
BEP	Building Effect Parameterization
BL	Bougeault–Lacarrere scheme
BLBEP	Bougeault–Lacarrere scheme coupled with BEP
CRMSE	Centered Root Mean Square Error
MAE	Mean Absolute Error
MBE	Mean Bias Error
MYJ	Mellor–Yamada–Janjic scheme
MYJBEP	Mellor–Yamada–Janjic scheme coupled with BEP
MYNN	Mellor–Yamada Nakanishi Niino- Level 3 Schemes
NCRMSE	Normalized Centered Root Mean Square Error
NMAE	Normalized Mean Absolute Error
PBL	Planetary Boundary Layer
PBLH	Planetary Boundary Layer Height
QNSE	Quasi–normal Scale Elimination scheme
R	Correlation Coefficient
UCM	single-layer urban canopy model
TKE	Turbulent Kinetic Energy
WRF	Weather Research and Forecasting model
YSU	Yonsei University scheme

Table 1
Summary of the studies on WRF PBL schemes cited in the Introduction with the corresponding acronym.

PBL scheme (Reference)	Acronym	Study
Asymmetric Convection Model 2 (Pleim, 2007)	ACM2	Avolio et al. (2017), Banks and Baldasano (2016), Banks et al. (2016), Chaouch et al. (2017), Gunwani and Mohan (2017), Sathyanadh et al. (2017), Xu et al. (2019)
Bougeault–Lacarrere (Bougeault and LaCarrere, 1989)	BL	Banks and Baldasano (2016), Banks et al. (2016), Sathyanadh et al. (2017), Xu et al. (2019)
Mellor–Yamada–Janjic (Janjic, 1994)	MYJ	Avolio et al. (2017), Banks et al. (2016), Chaouch et al. (2017), Gunwani and Mohan (2017), Sathyanadh et al. (2017), Xu et al. (2019)
Mellor–Yamada Nakanishi Niino-different levels (Nakanishi and Niino, 2006)	MYNN	Avolio et al. (2017), Banks and Baldasano (2016), Banks et al. (2016), Chaouch et al. (2017), Gunwani and Mohan (2017), Sathyanadh et al. (2017), Xu et al. (2019)
Quasi–normal Scale Elimination (Sukoriansky et al., 2005)	QNSE	Avolio et al. (2017), Banks et al. (2016), Chaouch et al. (2017), Gunwani and Mohan (2017)
Yonsei University (Hong et al., 2006)	YSU	Avolio et al. (2017), Banks and Baldasano (2016), Banks et al. (2016), Chaouch et al. (2017), Gunwani and Mohan (2017), Sathyanadh et al. (2017), Xu et al. (2019)
University of Washington (Bretherton and Park, 2009)	UW	Banks et al. (2016), Sathyanadh et al. (2017), Xu et al. (2019)
Total energy–mass flux (Angevine et al., 2010)	TEMP	Banks et al. (2016)
Grenier-Bretherton-McCaa (Grenier and Bretherton, 2001)	GBM	Chaouch et al. (2017), Xu et al. (2019)

while it is better for ACM2 and YSU according to Avolio et al. (2017).

None of the studies cited above considered urban canopy parameterizations, that are essential in mesoscale modeling to take into account the effects of buildings on wind and turbulent structures, though it was suggested in some studies (Avolio et al., 2017; Banks et al., 2016). WRF also includes different urban scheme options, specifically designed to represent atmosphere-city interactions in terms of thermal energy and momentum. In particular, the multi-layer Building Effect Parameterization (BEP, Martilli et al., 2002) computes the contribution of single urban surfaces (roofs, streets and facades of buildings) to the wind speed, temperature and turbulent kinetic energy. There are now plenty of studies focused on the modeling of urban areas and related phenomena (such as the urban heat island, heat waves, air quality) which are based on the application of these schemes; in Europe, for example: Madrid (de la Paz et al., 2016), Rome (Ciancio et al., 2018), Milan (Falasca et al., 2021), L'Aquila (Falasca and Curci, 2018), Berlin (Kuik et al., 2016; Li et al., 2019), Lisbon (Teixeira et al., 2019), Athens (Giannaros et al., 2013), and Turin (Ferrero et al., 2018).

In this study, we focused on the port-industrial site of Civitavecchia, located in the Central Mediterranean, on the coasts of the Tyrrhenian Sea, about 100 km north-west of Rome. It is one of the most important ports in Italy and the Mediterranean. Despite numerous past and ongoing initiatives aiming at reducing ship traffic and associated local transport emissions in port areas, these still represent an air quality and health problem (Matthias et al., 2010; Querol et al., 2017). Study of the atmospheric dynamics in such areas can help design mitigation strategies to keep pollutants levels within the standards imposed by the regulations in force and/or to protect the health of people living and working in the area and to preserve local ecosystems. In a recent investigation, Gobbi et al. (2020) showed that, although EU-regulated air quality limits are mostly met in the Civitavecchia area, constant consideration of an enlarged set of atmospheric variables, particularly ultrafine and black carbon particles loads, should drive more specific actions to mitigate the impact of the port emissions onto the port and the nearby city's air quality.

Models represent a useful tool to investigate impact scenarios but since outputs of numerical weather models (e.g., WRF) are used as driver for chemistry and transport models (e.g., CHIMERE), the evaluation of their skills in complex sites like Civitavecchia are crucial.

The wind dynamic along this coast is characterized by the presence of land – sea breeze and a periodic low-level jet that blows at a height of up to 600 m (Petenko et al., 2020). Previous modeling studies on wind dynamics in the Mediterranean, and in particular in Tyrrhenian coasts, highlighted critical issues in simulating coastal locations with respect to inland ones and correctly capturing the features of the local dynamics, such as the sea breeze circulation (Gioli et al., 2014; Tyagi et al., 2018). Most of those studies addressed a local circulation regime, such as land-sea breeze (e.g., Ferretti et al., 2003; Avolio et al., 2017) and low-level jet (e.g., Petenko et al., 2011). Overall findings indicated a high specificity of the performances of the model and the configurations used with respect to the geographic area. This work aims at providing a comprehensive investigation on the skills of the WRF model PBL schemes in resolving the circulation in the complex coastal region of Civitavecchia. Its main novelty consists in: 1) covering two local circulation regimes in addition to the synoptic regime and 2) the application of the Building Effect Parameterization (BEP) urban scheme.

Here we considered six WRF PBL schemes (four local and two non-local). The BEP scheme was applied in order to investigate the effect of the anthropic environment on temperature and wind speed and to evaluate its influence in a medium-size city context. The results were compared against recorded data of surface and near-surface meteorological quantities (temperature, wind speed intensity and direction, solar radiation). Temperature and wind speed were also measured at 120 m height.

The article is organized as follows: in Section 2 we present the site and the measurement instrumentation, the WRF setup and numerical experiments, the statistical parameters employed to evaluate the WRF results. Results are presented and discussed in Section 3, while Section 4 is focused on the conclusions.

2. Materials and methods

2.1. Monitoring site

Civitavecchia is a coastal site in central Italy, located about 100 km North-West of Rome (Fig. 1). Its port, founded by the emperor Trajan in 108 CE as the gateway to Rome, has represented for many centuries the core of exchanges and contacts between populations of the ancient “Mare Nostrum” (official site, https://www.portidiroma.it/pagina10308_porto-di-civitavecchia.html, in Italian). Thanks to its geographical and geophysical characteristics, it still plays a key role for maritime transport in the Mediterranean, linking Italy to Europe, North Africa and the Middle East. Today, Civitavecchia is the first cruise port in Italy and the second in Europe, and it is therefore affected by intense transport of atmospheric pollutants.

In addition to the port, the Civitavecchia area hosts the industrial sites of Torrevaldaliga North and Torrevaldaliga South: the first one consists in a coal-fired thermoelectric plant with a total power of 1980 MWe, is located about 6 km north of the port of Civitavecchia and has a surface area of 975,000 m^2; the latter consists of two combined cycle units based on natural gas-powered turbines for a total power of 1200 MW.

2.2. Measurement instruments and data

In April 2016, the ISAC-CNR AERosol mObile LABoratory (AEROLAB) was installed in the port of Civitavecchia, at Pier 24 (e.g., Fig. 1), in the framework of the AIRSEALAB project (Gobbi et al., 2020).

AEROLAB was set up to carry out in situ measurements of aerosol size distribution and optical properties, and aerosol vertical profiles by remote sensing but main meteorological variables were also recorded.

In addition, a Lufft AWS 700 weather station was installed on the roof of the AEROLAB vehicle (about 5 m above the ground) to measure meteorological parameters (namely P, T, RH, Ws, Wd and short-wave irradiance, with the temporal resolution of 1 min).

Overall, the meteorological instrumentation located in the Civitavecchia port area and used for this work is summarized in Table 2 together with the examined variables, and consists in:

- The AEROLAB weather station at Pier 24 (hereinafter, “P24”)
- meteo measurements located at two different heights on the Torrevaldaliga Nord thermal power plant (hereinafter, “TVN”) measuring temperature, wind speed and direction (biassial sonic anemometer Delta Ohm), solar radiation.

2.3. Measurement campaign and identification of atmospheric flow regimes

The meteorological observational data used in this study to evaluate WRF skills have been collected during a measurement campaign performed in the month of April 2016, with the main goal of investigating vertical wind velocity profiles, the height of the turbulent layer and the thermal structure of the atmosphere.

In order to better separate the effects of regional vs. large-scale

Table 2
Equipment, meteorological variables recorded and heights for each measurement site.

Site	Equipment	Meteorological variable	Heights (m) (a.s.l.)
Pier 24 (P24)	Lufft AWS 700 weather station	Temperature, Wind Speed, Wind Direction	10
Torre Valdaliga Nord (TVN)	Meteo	Temperature, Wind Speed, Wind Direction, Solar radiation	Temperature: 2.5 m (LSI LASTEM) and 120 m, Wind Speed: 10 m and 120 m, Radiation: 3 m (LSI LASTEM)

Fig. 1. The Civitavecchia port area and location of monitoring sites. The inset on the top right shows location of the Civitavecchia area with respect to the Rome city (Credits: background picture from Google Earth).

forcing on local atmospheric dynamic near the surface, we split the dataset into three subsets: the low-level jet (LLJ) regime and the land-sea breeze regimes, which are two main recognizable local-scale wind patterns, and a third collecting all the rest of the days, which we classified as “synoptic” regime, i.e. when wind is mainly conditioned by large-scale circulation systems.

According to the description in Stull (2018), the formation of the LLJ may take place when the isobars of sea-level pressure are perpendicular to a west-looking coastline, with a mountain range parallel to the coast, with high pressure located to the South and a low pressure to the North. With this topographical and air pressure pattern, the cold air on the sea is pushed northward along the coast and the mountain range, accelerating up to considerable velocity. Starting from the definition of LLJs characteristics from Bonner (1968), LLJ is a prevalent nocturnal wind with daily wind speed over 12 m/s that decreases with height. Subsequent revisions in Hodges and Pu (2019) classify LLJ like a wind with daily wind speed maximum of 12 m/s or greater at/or below 800 hPa that decrease at least 1 m/s between LLJ's core and 775 hPa. The presence of the LLJ on the Mediterranean Sea has been studied for a decade (e.g., Mastrangelo et al., 2011; Petenko et al., 2020); the LLJ present on the Tyrrhenian coasts develops in particular meteorological conditions when a high pressure is present in the southern part of Italy (preferably centered on the Gulf of Naples) and a low pressure is present in the northern areas of the country (Fig. 2a, b). We identified the LLJ

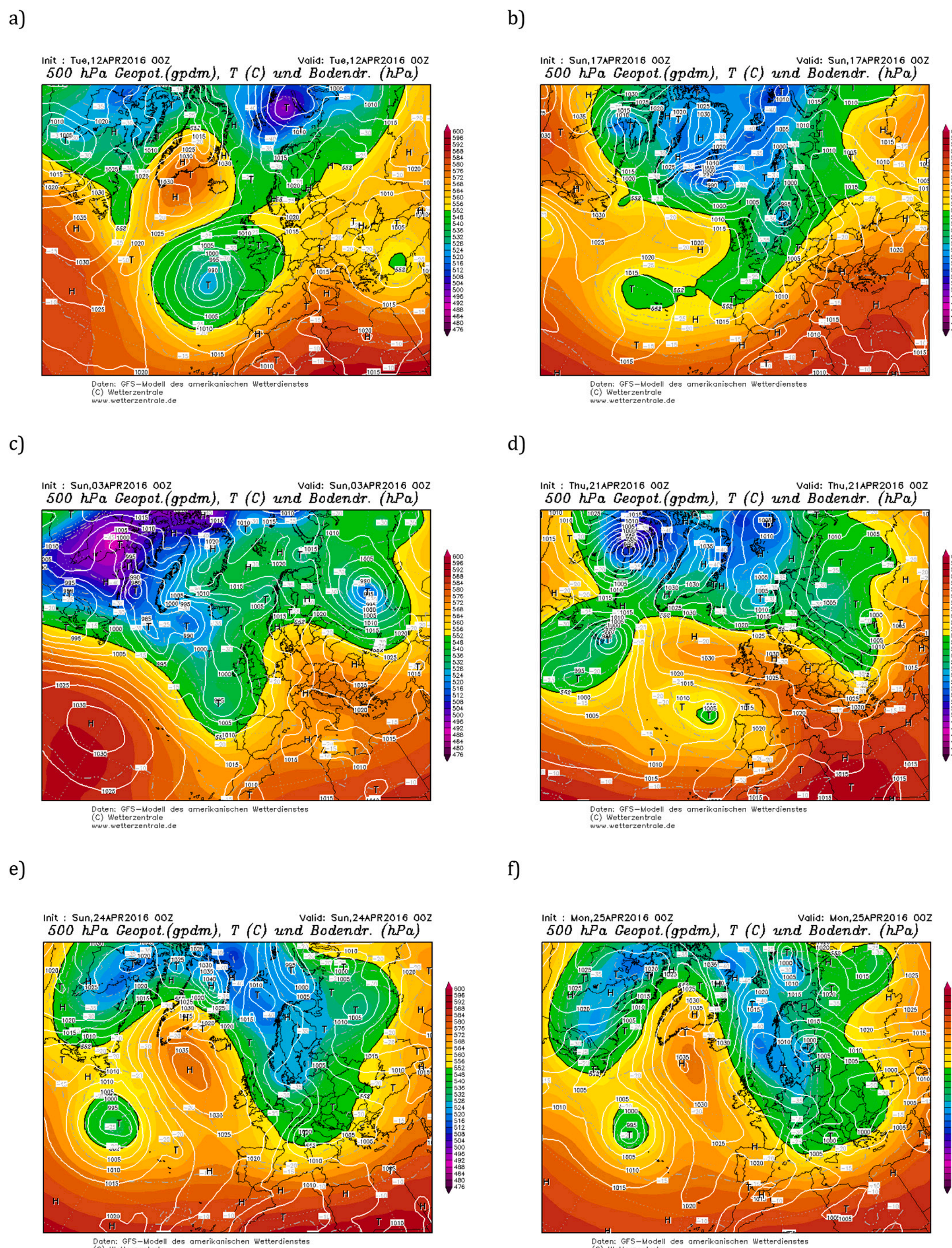

Fig. 2. An example of two sea-level pressure (white lines) and 500 hPa Geopotential (colors) map for jet (first row), breeze (second row), synoptic regime (third row): (a) 12th, (b) 17th, (c) 3rd, (d) 21st, (e) 24th, (f) 25th April 2016.

days using SODAR vertical profiles, founding a maximum altitude of 1000 m and speeds between 10 and 15 m/s (Petenko et al., 2020).

The land-sea breeze regime may be present along all Italian coasts and it mainly arises when a difference of about 5 °C is present between the land and the sea (Stull, 2018). The breeze is a local manifestation of the presence of a confined low pressure on the land near the shoreline and a corresponding high pressure on the sea, so the wind blows from the sea to the land during daytime. Due to the different thermal capacities of land and sea, at night the breeze reverses its direction blowing from the land to the sea. The presence of this regime is possible when the sites are affected by an extended high pressure that allows meteorological stability and reduced large-scale forcing (Fig. 2c, d). From the SODAR and the near-surface weather station (Section 3.1.4) it is possible to identify the breeze with the typical clockwise rotation of the wind direction during the day.

We show examples of the third "synoptic" regime in Fig. 2e, f: these are all the other days when large-scale forcing predominates over local-scale processes, such as at the passage of a meteorological front or of a low pressure system.

On the basis of the definitions provided by Stull (Bonner, 1968; Stull, 2018) and through SODAR profiles, Petenko et al. (2020) identified seven days during April 2016 characterized by LLJ. The land- sea breeze regime has been identified based on the low wind speeds and on the typical daily clock-wise rotation of the winds near the surface. The remaining days are classified as "synoptic regime", when wind dynamic is driven by large-scale circulation systems. Table 3 lists the days of the measurement campaign characterized by each regime.

2.4. PBL schemes and numerical experiments

The role of the PBL schemes in WRF is to compute the flux profiles within both the well-mixed and stable boundary layers, and to provide tendencies of temperature, moisture and momentum (Skamarock et al., 2019). A total amount of twelve PBL parameterization schemes are now embedded in the WRF model, characterized by a different type of closure (local, non-local, hybrid non-local) and a different order of turbulent closure (first-order, one-and-a-half, second order). In this study, we tested the following six PBL schemes using proper surface layer schemes: Asymmetric Convection Model 2 (ACM2), Bougeault–Lacarrere (BL), Mellor–Yamada–Janjic (MYJ), Mellor–Yamada Nakanishi Niino- Level 3 Schemes (MYNN), Quasi–normal Scale Elimination Scheme (QNSE), Yonsei University (YSU). Furthermore, we coupled two of them with the BEP urban scheme keeping default values of thermo-physic urban properties, for a total of eight numerical experiments. A brief description of the PBL urban schemes used in this work is provided, while for a detailed description of the PBL schemes embedded in WRF the reader is referred to reviews by Cohen et al. (2015) and Jia and Zhang (2020).

The ACM2 (Pleim, 2007) represents an evolution of the original ACM ("a simple transilient model") combining the non-local scheme of ACM with an eddy diffusion scheme. In particular, an eddy diffusion component is added to the non-local transport. This combination makes the ACM2 able to represent both large and subgrid turbulent structures under convective conditions, going beyond the limitations of local and non-local closure schemes in modeling convective boundary layers. In this sense, ACM2 is defined as a hybrid local-nonlocal closure. Nevertheless, most of literature categorizes ACM2 as a non-local scheme and for the sake of comparison with other studies such classification is

Table 3
Days of the measurement campaign characterized by each regime.

Regime	Days of April 2016	Total days
Breeze	2, 3, 6, 7, 9, 14, 21	7
Low Level Jet	1, 4, 5, 12, 13, 16, 17	7
Synoptic	8, 10, 11, 15, 18, 19, 20, 22, 23, 24, 25, 26, 27, 28, 29, 30	16

adopted also in this work. In this model, the realistic modeling of the vertical mixing is crucial not only for meteorological application, but also for air quality applications (Pleim, 2007). The YSU is a non-local first order scheme. It is based on the Medium-Range Forecast (MRF) scheme modified with the inclusion of an explicit treatment of the entrainment process of heat and momentum fluxes at the inversion layer according to the outcomes of Noh et al. (2003). In more detail, an additional term is present on the right hand side of the turbulence diffusion equation for prognostic variables making explicit the entrainment flux term at the inversion layer. Above the mixed layer, the free atmospheric diffusion is modeled through a local diffusion scheme. Most of local schemes, namely MYJ, BL, MYNN and QNSE are based on the second-order Mellor-Yamada model and have been designed to improve shortcomings of the original Mellor Yamada version (e.g., the underestimations of the mixed-layer depth and the magnitude of turbulent kinetic energy). BL (Bougeault and LaCarrere, 1989) and MYJ (Janjic, 1994) present a 1.5 order closure with a prognostic equation of the turbulent kinetic energy (TKE) and both schemes have been adjusted to be coupled with BEP. The QNSE has been designed for stratified boundary layers (Sukoriansky et al., 2005). It is a spectral closure-based $k-\varepsilon$ model, built on of Mellor-Yamada type formulation with modified expressions of the eddy-transfer coefficients. The two MYNN schemes (Nakanishi and Niino, 2006, 2009), MYNN2.5 and MYNN3, include respectively the prognostic equation of TKE and of second-order moments.

The Building Effect Parameterization BEP is a multilayer layer scheme parameterizing the effects of the urban structures on the overlying atmosphere. The purpose of the scheme is to quantify the influence of each urban element from a dynamic, turbulent and energetic point of view. That is on momentum, TKE and heat. In particular, a loss term is introduced in the momentum equation and a source term in TKE equation, both depending on the wind speed (the square and the cube, respectively), a drag coefficient and the buildings density. Moreover, shadowing and radiation trapping effects are taken into account in the computation of the radiation. The urban texture is schematized and specific sizes and properties are provided as default values or can be modified by the user. The BEP urban scheme is extensively explained in Martilli et al., 2002.

The features of the numerical experiments performed are listed in Table 4, together with the references of the PBL schemes.

2.5. Setup of the Weather Research and Forecasting model

In this study, we used the mesoscale Weather Research and Forecasting (WRF) model, version 4.1.2. For the technical description of WRF, the reader is referred to Skamarock et al. (2019).

Four one-way nested domains are cut with increasing horizontal resolution from 36 km to 1.3 km and a grid ratio of 4 (Fig. 3a). The configuration includes 33 vertical levels with 11 levels below 1000 m, the lowest at around 23 m and the top corresponding to 50 hPa. Physics options used in the numerical experiments are listed in Table 5. The initial and global boundary conditions are supplied by the operational analyzes of the Global Forecasting System (GFS) of the National Center for Environmental Prediction (NCEP), with a spatial resolution of 1°x1° and a temporal resolution of 6 h (https://www.ncdc.noaa.gov/data-access/model-data/model-datasets/global-forcast-system-gfs). Our runs consist of blocks of 30 h, starting at 18 UTC every day and discarding the first spin-up 6 h. Supplementary runs (not shown here) aimed at testing the two-way nesting technique, a longer spin-up and a longer total duration demonstrated a negligible influence on model results.

The land use database is derived from MODIS satellite observations. Fig. 3a shows the categories of the innermost domain grouped in four classes: water, cropland (non-urban), mixed forest (non-urban) and urban. The pink markers represent the monitoring sites: the triangle for P24 and the circle for TVN, both cells are classified as urban. Fig. 3b

Table 4
Features of the numerical experiments: PBL schemes (and references), type and order of closure, surface layer schemes (and references), urban scheme (and reference) and corresponding label.

PBL scheme (Reference)	Type of closure	Order of closure	Surface layer	Urban scheme		Label	
Asymmetric Convection Model 2 (Pleim, 2007)	Hybrid	1	Revised MM5 Monin-Obukhov	–		ACM2	
Bougeault–Lacarrere (Bougeault and LaCarrere, 1989)	Local	1.5	Revised MM5 Monin-Obukhov	–	BEP (Martilli et al., 2002)	BL	BLBEP
Mellor–Yamada–Janjic (Janjic, 1994)	Local	1.5	Monin-Obukhov (Janjic Eta) scheme	–	BEP (Martilli et al., 2002)	MYJ	MYJBEP
Mellor–Yamada Nakanishi Niino- Level 3 Schemes (Nakanishi and Niino, 2006, 2009)	Local	2	MYNN surface layer	–		MYNN	
Quasi–normal Scale Elimination Scheme (Sukoriansky et al., 2005)	Local	1.5	QNSE surface layer	–		QNSE	
Yonsei University (Hong et al., 2006)	Non local	1	Revised MM5 Monin-Obukhov	–		YSU	

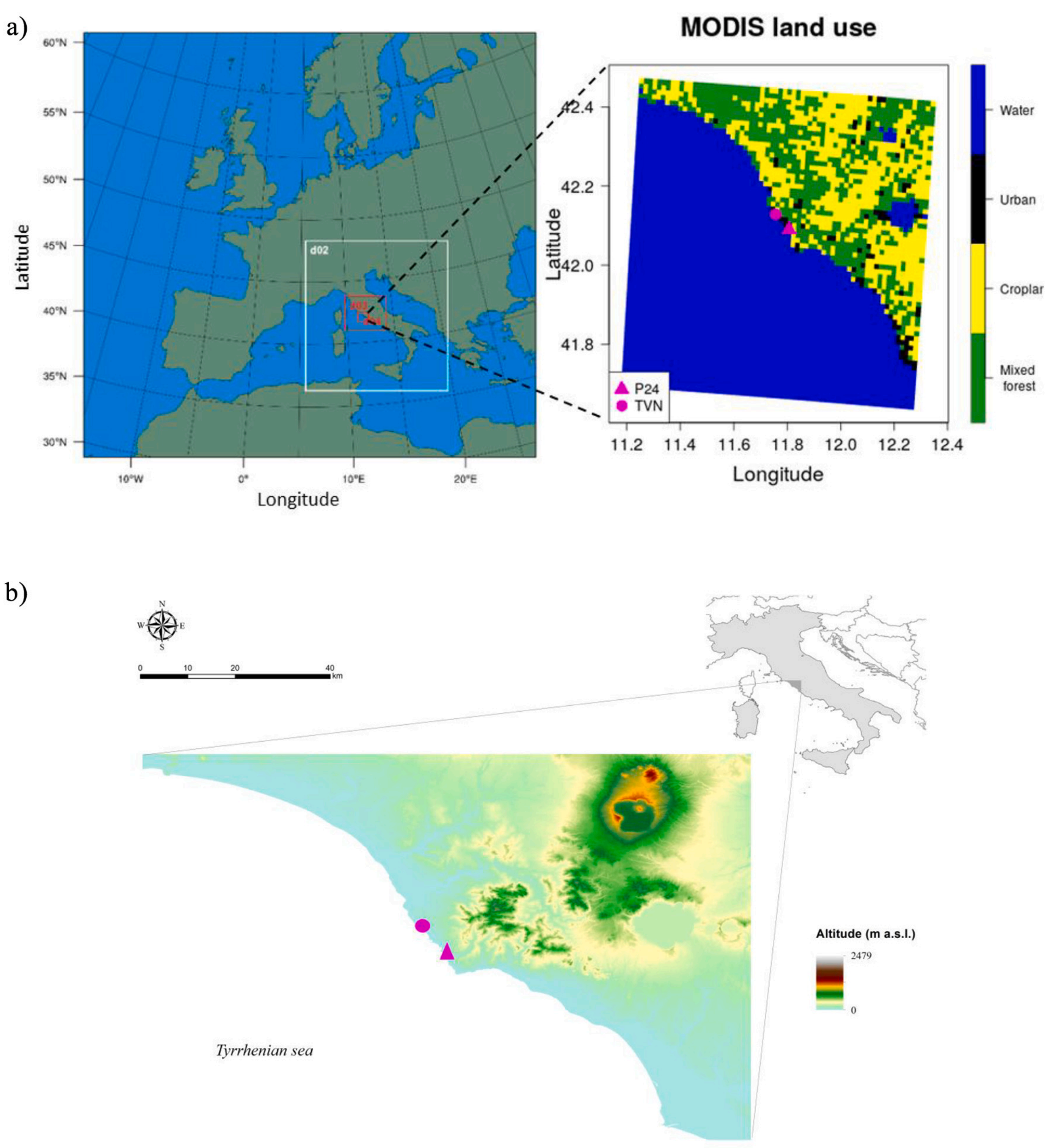

Fig. 3. (a) Four nested domains used for WRF simulations and MODIS land use in the innermost domain. (b) Topographic map of the innermost domain. Pink markers represent the monitoring sites (the triangle, P24 and the circle, TVN). (For interpretation of the references to colour in this figure legend, the reader is referred to the web version of this article.)

Table 5
List of physics options used in the numerical experiments.

Category	Option
Microphysics	WSM6
Long wave radiation	RRTMG scheme
Shortwave radiation	RRTMG scheme
Land Surface	Unified Noah land-surface model
Surface Layer	See Table 4
Planetary Boundary Layer	See Table 4
Urban Physics	See Table 4

shows the topography of the fourth domain.

2.6. Statistical analysis

The statistical analysis is carried out by comparison of the observed and simulated data at the instrumented sites described in Section 2.2. We computed the mean bias error, the mean absolute error and the normalized mean absolute error, for the three regimes and differentiating among daytime (from 06:00 to 17:00) and nighttime (from 18:00 to 05:00). Some of statistics are also illustrated over Taylor diagrams. We used the "applystat" function of the R "tdr" package (Lamigueiro, 2018) and the "TaylorDiagram" function of the R "openair" package (Carslaw and Ropkins, 2012; Carslaw, 2015).

The statistical parameters used in this statistical analysis are defined as follows (Emery et al., 2017):

- Mean Bias Error (MBE):

$$MBE = \frac{1}{N}\sum\left(P_j - O_j\right)$$

- Mean Absolute Error (MAE):

$$MAE = \frac{1}{N}\sum\left|P_j - O_j\right|$$

- Centered Root Mean Square Error (CRMSE, Thunis et al., 2011):

$$CRMSE = \sqrt{\frac{1}{N}\sum\left[\left(P_j - \overline{P}\right) - \left(O_j - \overline{O}\right)\right]^2}$$

- Normalized Mean Absolute Error (NMAE):

$$NMAE = \frac{1}{N}\sum\frac{\left|P_j - O_j\right|}{O_j}\bullet 100$$

- Correlation coefficient (R):

$$R = \frac{\sum\left[\left(P_j - \overline{P}\right)\bullet\left(O_j - \overline{O}\right)\right]}{\sqrt{\sum\left(P_j - \overline{P}\right)^2\bullet\sum\left(O_j - \overline{O}\right)^2}}$$

Where:

- O represents observations
- P represents predictions
- Overbars signify the mean over time

The Taylor diagram (Taylor, 2001) is a compact tool that displays simultaneously the values of three statistical parameters: the correlation coefficient (R), the standard deviation (sigma) and the centered root mean square error (CRMSE). In particular, in this version of the graph both the standard deviation and the CRMSE of the model are normalized with respect to the corresponding values of the observations. In these diagrams the perfect match of a model with the observations would be the point with coordinate $R = 1$, normalized $\sigma = 1$ and normalized CRMSE $= 0$.

3. Results and discussion

We compared the results of the numerical experiments against the observations at the monitoring sites described in Section 2.1 for incoming solar radiation, temperature (2.5 m, 10 m and at 120 m), wind speed intensity (10 m and at 120 m) and wind speed direction. The analysis is presented according to the subdivision of the measurements into the three regimes and time periods introduced in Section 2.3. The observations are colored in black and the numerical experiments in different colors, using solid lines for non-local PBL schemes, dashed lines for local PBL schemes and markers for BEP configurations.

3.1. Surface and near-surface variables

3.1.1. Solar radiation

The average daily time series of the incoming solar radiation (Fig. 4) show that all the numerical experiments provide very similar values on breeze days, slightly higher than the observations. At P24 the MYNN case presents the minimum daily values of MBE (Table 6) and MAE (Table 7) and, equal to 82 and 34 W m^{-2} respectively, corresponding to a NMAE of 0.094 (Table 7). The MYNN schemes has the highest skills also at the TVN site, with MBE and MAE equal to 52 and 81 W m^{-2} respectively and NMAE equal to 0.094. During the night, WRF provides null values of solar radiation, whereas the instruments detect small but not null values due to artificial light, both at P24 and TVN.

During the jet and synoptic regimes all the PBL schemes except MYNN simulate the same incoming shortwave radiation values, overestimated with respect to the observations. The MYNN scheme, on the other hand, matches pretty well the average daily cycle of the observations. During jet days, the values of daily MBE (Table 6) are between −11 W m^{-2} of MYNN and 69 W m^{-2} of MJY at P24, whereas they are slightly higher at TVN (between 20 and 94 W m^{-2}). During synoptic days, MYNN and QNSE are characterized by the minimum and maximum values of MBE that goes from 18 W m^{-2} to 92 W m^{-2} at P24 and from 26 W m^{-2} to 84 W m^{-2} at TVN (Table 6). The deviation of the MYNN results from the other PBL schemes can also be observed in the 2 m and 120 m temperature graphs. A further investigation (not shown) indicated that the MYNN case presents an attenuation of the shortwave down welling flux at bottom with respect to the clear sky conditions. Furthermore, the comparison with other cases shows that the MYNN case simulates lower values of shortwave down welling flux at bottom.

Taylor diagrams confirm the solid WRF-observations agreement during daytime shown by the time series (Fig. 5) and by the statistical metrics in Table 6 and Table 7. NCRMSE is always below 0.8 at P24, with the minimum correlation coefficient equal to 0.75 and the normalized standard deviation close to 1. The agreement is very good also at TVN, even with a lower NCRMSE than at P24, with correlation higher than 0.8 and the normalized standard deviation close to 1.

For this parameter, model to observations comparison is not meaningful for the nighttime since the solar radiation at night is absent.

3.1.2. Temperature

Fig. 6 shows the temperature (at 2 m height) time series averaged for each regime and site, for both observations and numerical experiments. The spatial distribution of temperatures shown in Fig. 3S and Fig. 4S (supplementary material) reflects the topography of the geographical area in the innermost WRF domain (see Fig. 3). The mountains are especially recognizable near the coast and in the north-eastern part of the domain (in proximity of a small lake). The average diurnal

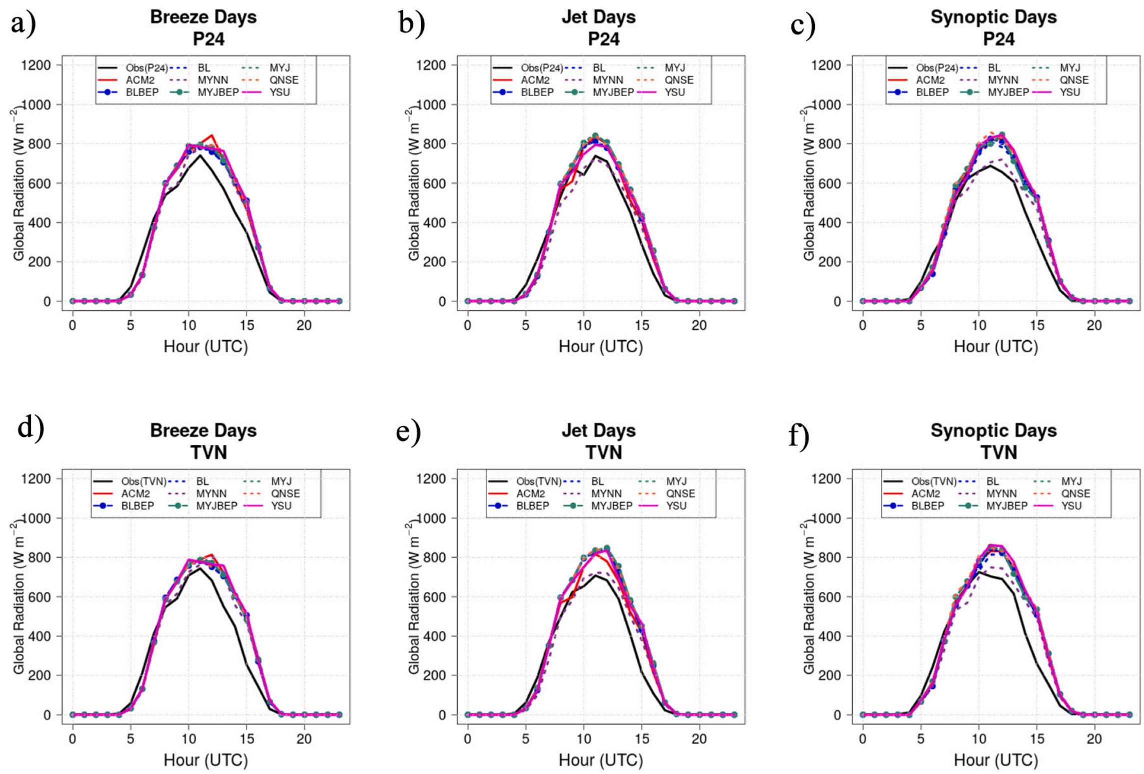

Fig. 4. Average daily time series of incoming solar radiation for P24 (first row) and TVN (second row) for the three regimes.

Table 6
Mean Bias Error (MBE) for incoming solar radiation in (W m^{-2}).

	Breeze		Jet		Synoptic	
Label	P24	TVN	P24	TVN	P24	TVN
ACM2	57	72	42	63	78	68
BL	55	70	57	89	59	63
BLBEP	53	68	58	91	68	66
MYJBEP	62	69	69	99	86	75
MYJ	67	74	69	98	87	75
MYNN	34	52	−11	25	18	26
QNSE	65	72	67	95	92	84
YSU	66	77	48	82	82	77

temperature is lower in the synoptic regime than in the breeze and jet regimes over the whole domain, while the jet regime is characterized by intermediate temperatures between the synoptic and the breeze.

On breeze days, results of the eight experiments are very similar during the central hours of the day, while in the rest of the day the simulations have slight different results. Consistently with the maps, this behavior is especially apparent during nighttime and at TVN. As for the comparison with the observations, an opposite behavior is observed at P24 and TVN: at P24 the model-observations agreement worsens during the night, with a corresponding slight increase in the MAE, and a worsening in terms of correlation, NCRMSE and normalized standard deviation (see Taylor plot in Fig. 7a). On the other hand, at TVN there is an evident disagreement during daytime, with MAE and MBE decreasing for most cases during the night (Table 8 and Table 9). Furthermore, during the night WRF has better performances at TVN than at P24 in terms of MBE and MAE. Also according to Banks et al. (2016), coastal locations present the highest bias. During night, BLBEP overestimates temperature more than all the other cases and therefore presents the worst agreement with the observations (MBE equal to 2.2 °C at P24 and 1.9 °C at TVN, Table 8), in addition to a consistent increase of MAE and NMAE (Table 9) respect to daytime. During breeze nights, correlation strongly worsens in both sites; for example, the correlation is about 0.1 for BLBEP at TVN that is the poorest of all experiments (Fig. 7). We note that the temperature variability in those periods is relatively low (not shown), thus the correlation is a less meaningful quantity.

On jet days, modeled temperatures are lower than observed ones, both at P24 and at TVN. As for the breeze days, WRF results of local schemes are close to each other during the day but not at night. A

Table 7
Mean Absolute Error (MAE) and Normalized Mean Absolute Error (NMAE) for incoming solar radiation during breeze days.

	MAE				NMAE			
Label	P24		TVN		P24		TVN	
	Day	Night	Day	Night	Day	Night	Day	Night
ACM2	88.	3.7	101.	4.5	0.10	0.030	0.11	0.045
BL	90.	3.7	101.	4.6	0.10	0.030	0.11	0.045
BLBEP	90.	3.7	99.	4.5	0.10	0.030	0.11	0.045
MYJbep	94.	3.7	103	4.6	0.11	0.030	0.11	0.045
MYJ	97.	3.7	105.	4.6	0.11	0.030	0.11	0.045
MYNN	82.	4.2	95.	4.9	0.094	0.034	0.10	0.048
QNSE	99.	3.7	110.	4.6	0.11	0.030	0.12	0.045
YSU	100.	3.7	112.	4.6	0.11	0.030	0.12	0.045

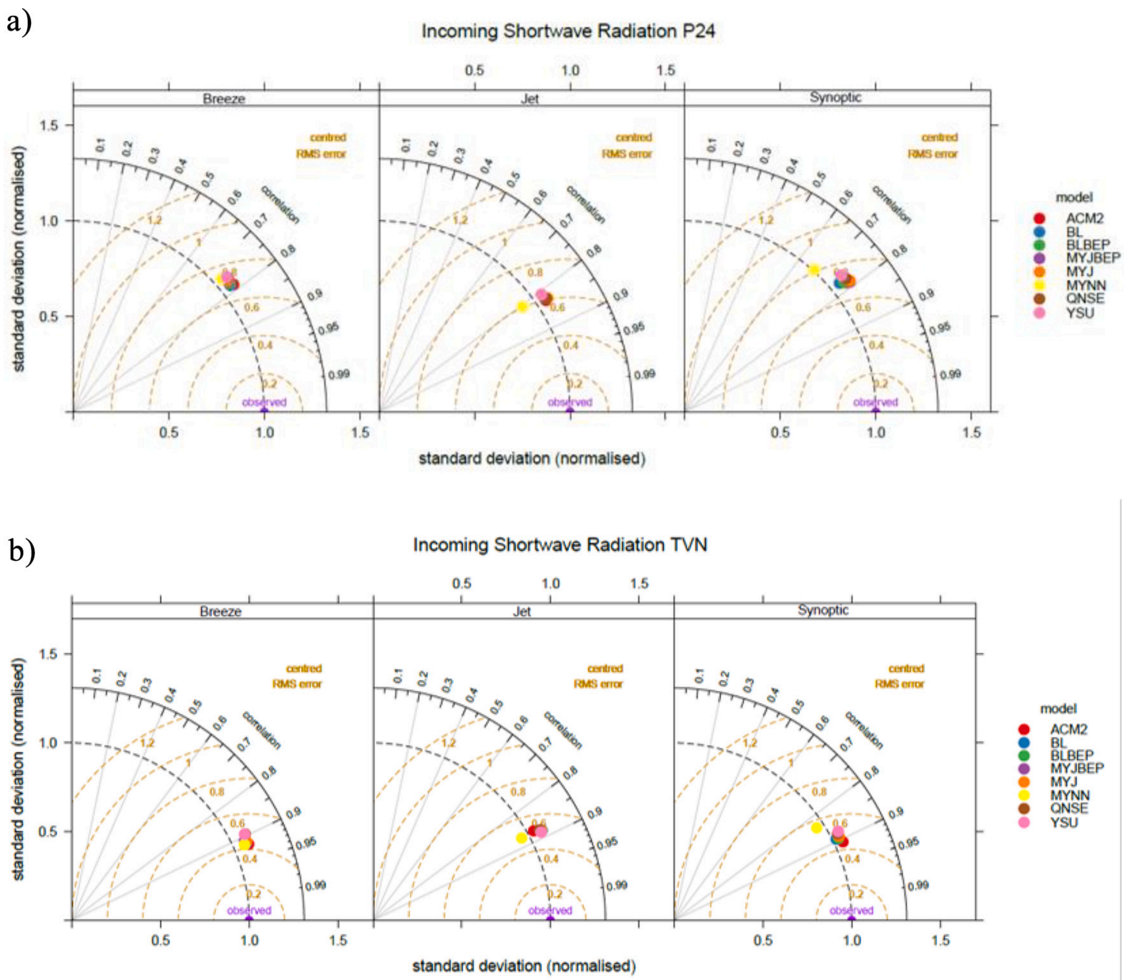

Fig. 5. Taylor plots for the solar radiation at P24 (left) and TVN (right). Simulated and observed data are grouped according to the regime (breeze, jet and synoptic) and for daytime.

plausible reason for this could be that nocturnal stability favors a differentiation of the results of the local schemes that are considered more suitable for stable flows (Jia and Zhang, 2020). The MYNN case falls outside this, as it provides significantly colder temperatures than other numerical experiments throughout the day, analogously to the incoming solar radiation. Indeed, at P24 it has a MBE equal to −2.6 °C and −2.8 °C during daylight and nighttime respectively, whereas the maximum bias for the other PBL schemes is equal to −1.6 °C and −2.1 °C (for QNSE, Table 8). Consistently with the 2 m temperature maps and the surface skin temperature time series (supplementary material), QNSE and MYNN have the coldest time series. As for the breeze days, the BLBEP case simulates higher values of temperature during the night, with a consequent decrease of MBE (from −1.5 °C of BL to −0.93 °C at P24 and from −1.7 °C of BL to 0.076 °C). This case has the worse correlation also during jet night at TVN (Fig. 7).

During the days characterized by synoptic flows, WRF underestimates the observations in terms of the average daily cycle at both monitoring sites. As for the breeze days, nighttime performances of WRF are slightly better at TVN than at P24 with lower absolute values of MBE and MAE. As for the daytime, there are more slight differences between P24 and TVN.

In order to better understand this behavior of the PBL schemes, we also investigated the surface energy budget and the surface temperature (shown both in the supplementary material). Contrary to the temperature, the surface energy balance is reproduced by the PBL schemes without significant differences in the three regimes. Also the MYNN scheme, which simulates colder temperatures, returns net energy flows just lower than those of ACM2, BL and MYJ and higher than that of QNSE especially at P24. Also the surface skin temperature is higher for MYNN than for QNSE but lower than for the other schemes. The fact that the temperature simulated by MYNN during jet days is much lower than the other cases, although this is not the case for the surface energy balance and the surface skin temperature, could be due to the soil-atmosphere interaction, as will be commented later in the section on wind. Schemes coupled with BEP (i.e. BLBEP and MYJBEP) simulate a net energy flux at the ground equal to each other and lower than the other schemes both at P24 and TVN. At P24, also the QNSE scheme simulates a net energy flux comparable to that of BLBEP and MYJBEP.

In Taylor plots of Fig. 7, NCRMSE is less than or equal to 1.5 for most of experiments (including the three regimes and both the monitoring sites).

The differences between BEP cases (BLBEP and MYJBEP) and the corresponding bulk cases (BL and MYJ) are shown in Fig. 5S and Fig. 6S of the supplementary material. For the BL case such difference is negligible almost everywhere in the domain except that in the urban cells that are particularly evident in the breeze regime. Also for the MYJ case images show that such difference assumes non-zero values for all regimes in the urban cells with no significant difference in the rest of the domain. Unlike the BL case, the use of the BEP scheme causes a temperature drop for MYJ in correspondence of the urban land-use. Even during night, the synoptic regime is the coldest one, while jet nights are the hottest. The spatial distribution of temperatures highlights the

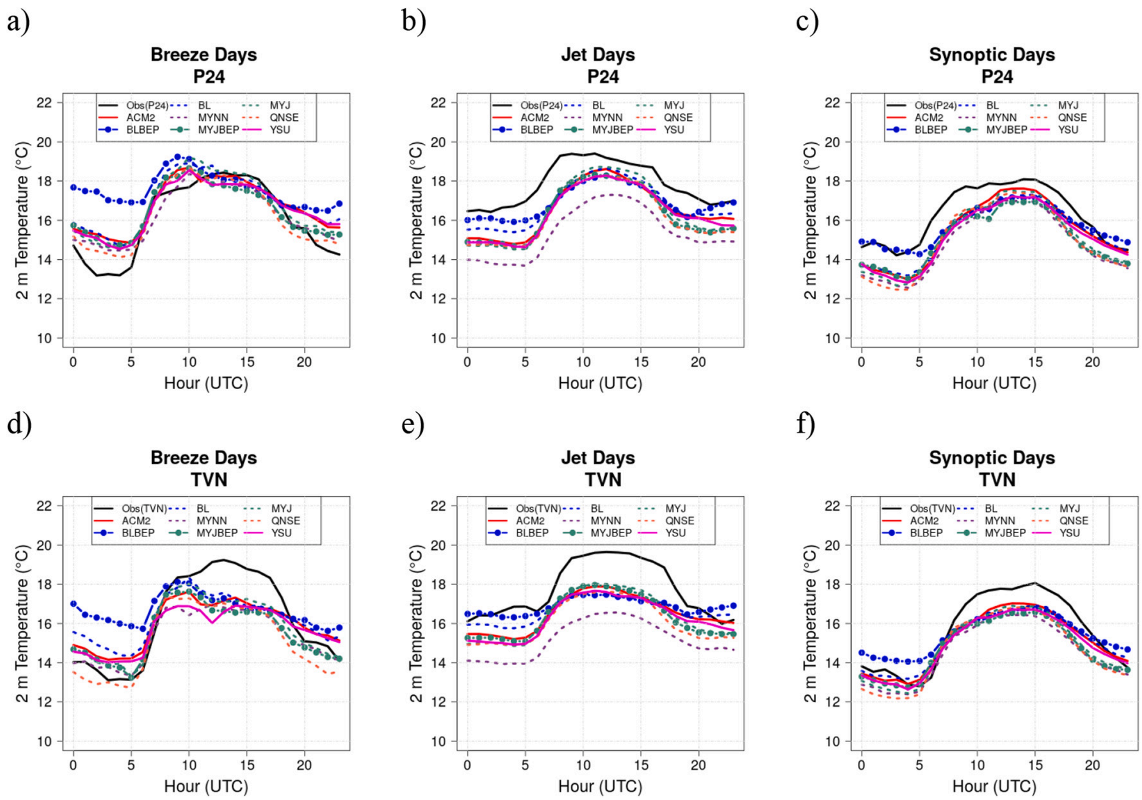

Fig. 6. Same as Fig. 4, but for temperature at 2 m height.

reliefs, as for the daytime. The coastal area (where the two measurement sites are located) is warmer than the neighboring areas and this phenomenon is represented in different ways by the PBL schemes. On breezy nights, this phenomenon is enhanced in the QNSE case, where the temperature on the coast is around 14–15 °C, while the most part of the remaining domain has a temperature of around 10 °C. Dissimilarities among the temperature maps are significant during jet nights and also during the synoptic nights temperature patterns vary with the PBL scheme. The temperature difference is nearly negligible for MYJ over the whole domain except for urban cells, characterized by small positive increases (i.e., MYJBEP> MJY). Even in the BL case such differences are positive, but more pronounced than in MYJ.

3.1.3. *Wind speed intensity*

The different PBL schemes spatially reproduce the intensity of the wind responding to the forcing derived from the topography of the territory (Fig. 3) and to the distance from the sea.

Fig. 8 shows a general tendency of the WRF model to overestimate the wind speed, consistently with a peculiarity of the WRF model already noticed in previous works, especially in case of complex topography (e.g., Ribeiro et al., 2018; Arrillaga et al., 2016). The penalizing effect of the topography in simulating the wind speed was also mentioned by Giannaros et al. (2013) and Jiménez and Dudhia (2012) ascribed such wind speed bias to "unresolved orographic features" whose effects are not included in WRF. In our results, jet days are characterized by the model's highest sensitivity to configurations both at TVN and P24 except for ACM2 and YSU, as for temperature results. The WRF curves depicted in Fig. 8 strongly overlap during breeze days, while they overlap less and slightly for the synoptic and jet days, respectively. This involves a considerable excursion of statistical metrics for jet days, when the daytime MAE varies between 2.1 m/s of MYJBEP and 5.2 m/s of MYJ at TVN; there is a slight excursion during breeze days, when the daytime MAE varies between 1.1 m/s of MYJBEP and 2.0 m/s of QNSE at TVN. Moreover, contrary to what was observed for temperature such sensitivity concerns the whole day and not mainly the night. Indeed, in the Taylor diagrams (Fig. 9) for jet days the markers of the different numerical experiments are located along the same radius (corresponding to $R = 0.8$), but they differ in terms of CRMSE and sigma.

Regarding the breeze days, the wind speed intensity is pretty uniform over the entire domain for all PBL schemes, with diurnal values ranging between 2 m/s and 7 m/s (Fig. 9S). All the parameterizations exhibit the same behavior for the breeze night: the wind speed drops to 0–5 m/s in the inland areas corresponding to the reliefs, probably due to valley-mountain breeze regimes that establish in the evening. QNSE, MYNN and MYJ schemes exhibit the highest ranges in intensity between daytime and night-time, as shown also in P24 and TVN time series (Fig. 8). Regarding the jet days, the wind speeds are generally higher than that on the breeze days on the whole domain, with intensity ranging between 3 m/s and 12 m/s during the day (Fig. 9S) and between 1 m/s and 12 m/s during the night (Fig. 10S). Such high intensity of the wind speed during jet days, additionally to the lower incoming radiation (Fig. 4), could explain the low temperature of the MYNN case (Fig. 6).

Contrary to breeze days, the jet is not affected by the day-night dynamics as expected. In the areas rising to a few meters above sea level the wind intensity values are lower than at the peaks and the maximum jet speeds are reached between 100 and 400 m a.g.l. (Stull, 2018; Zemba and Friehe, 1987; Garratt and Physick, 1985). As for breeze days, MYNN, MYJ and QNSE schemes provide the highest difference between diurnal and night values. The explanation could be found in the topography of the territory: a second circulation derived from both land-sea and valley-mountain breezes could be superimposed on the dynamics of the Jet.

As regards the days classified as "synoptic", during daytime the wind speed intensity is basically uniform over the domain with values between 4 m/s and 6 m/s. During night-time, all PBL schemes simulate lower wind intensities with values between 2 m/s and 5 m/s., with the highest values found in the internal areas in correspondence with the reliefs. Marked differences between diurnal and night values can be

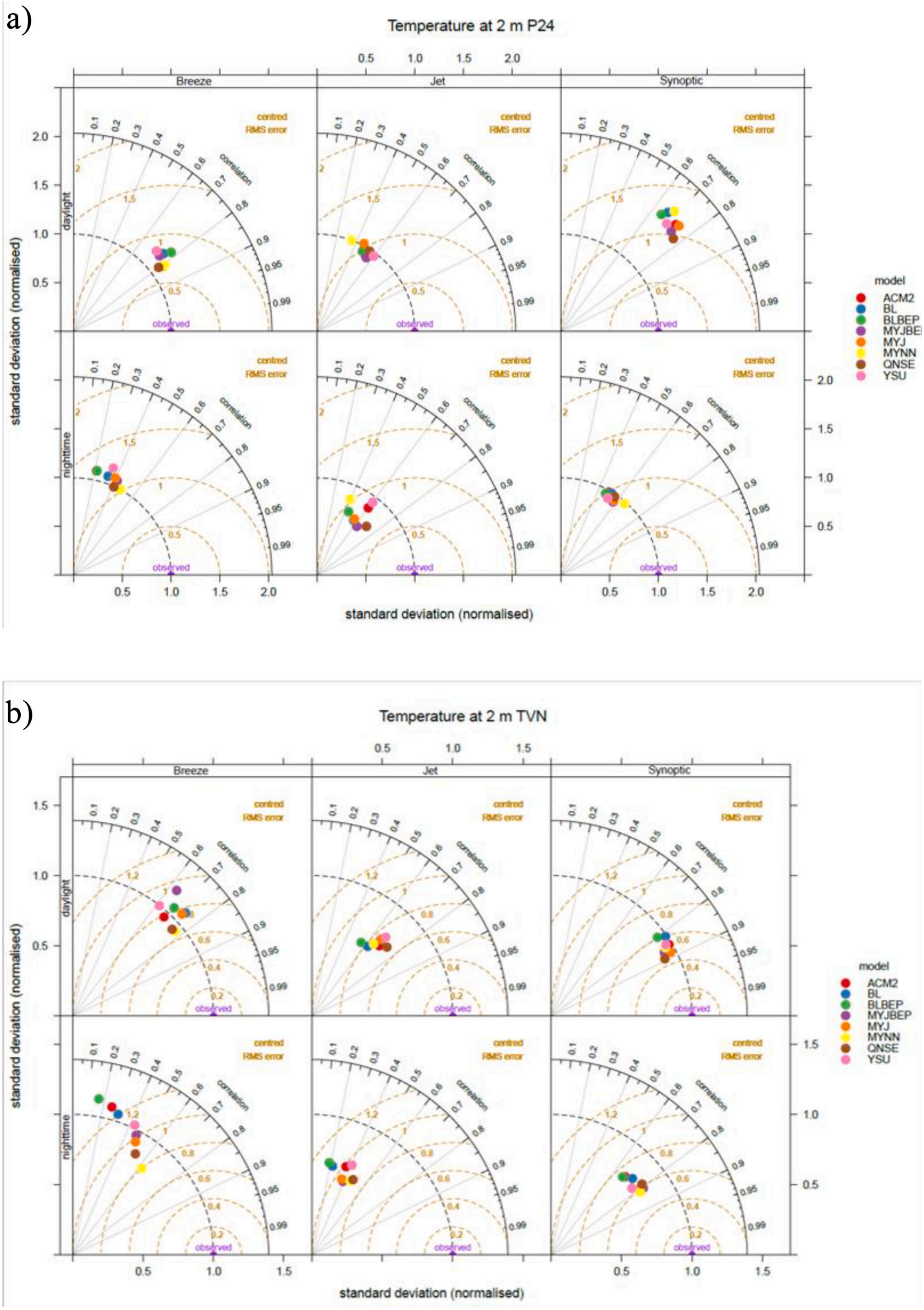

Fig. 7. Taylor plots for the temperature at 2 m height at P24 (left) and TVN (right). Simulated and observed data are grouped according to the regime (breeze, jet and synoptic) and for time slot (daytime, nighttime).

identified for the ACM2, QNSE and MYNN schemes, while the YSU scheme provide comparable values between day and night. An additional test not included in this work demonstrated that coupling of MYNN with the single-layer Urban Canopy Model UCM (MYNN cannot be coupled with BEP) has negligible effects on the simulation of wind speed during jet and synoptic days and causes a further overestimation of the values observed during breeze days at both sites. On the contrary, Feng et al. (2016) found that UCM coupled PBL schemes were

Table 8
Mean bias error (MBE) for 2 m temperature during breeze days.

Label	Breeze				Jet				Synoptic			
	P24		TVN		P24		TVN		P24		TVN	
	D	N	D	N	D	N	D	N	D	N	D	N
ACM2	−0.63	0.79	−1.0	0.75	−1.4	−1.7	−1.6	−0.78	−0.36	−0.57	−0.71	−0.13
BL	−0.56	0.89	−0.81	0.97	−1.3	−1.3	−1.7	−0.39	−0.61	−0.30	−0.79	0.032
BLBEP	−0.31	2.2	−0.75	1.9	−1.5	−0.93	−1.7	0.076	−0.53	0.38	−0.71	0.66
MYJBEP	−0.97	0.68	−0.95	0.14	−1.5	−2.0	−1.6	−1.2	−0.85	−0.65	−1.0	−0.54
MYJ	−0.51	0.65	−1.3	0.052	−1.2	−2.0	−1.6	−1.1	−0.54	−0.81	−0.87	−0.62
MYNN	−1.2	0.49	−1.5	−0.074	−2.6	−2.8	−2.9	−2.1	−1.0	−1.13	−1.2	−0.80
QNSE	−0.83	−0.036	−1.4	−0.77	−1.6	−2.1	−1.9	−1.4	−0.67	−1.11	−0.95	−0.96
YSU	−0.89	0.77	−1.4	0.60	−1.6	−1.9	−1.8	−1.1	−0.70	−0.65	−0.92	−0.32

Table 9
Mean Absolute Error (MAE) and Normalized Mean Absolute Error (NMAE) for 2 m temperature during breeze days.

Label	MAE				NMAE			
	P24		TVN		P24		TVN	
	Day	Night	Day	Night	Day	Night	Day	Night
ACM2	1.4	2.3	1.7	1.7	0.15	0.33	0.19	0.22
BL	1.4	2.1	1.6	1.7	0.15	0.30	0.18	0.22
BLBEP	1.5	2.5	1.8	2.2	0.16	0.36	0.20	0.28
MYJBEP	1.6	1.8	1.6	1.2	0.17	0.27	0.17	0.15
MYJ	1.1	1.9	2.0	1.2	0.12	0.28	0.22	0.16
MYNN	1.5	1.7	1.8	1.0	0.16	0.25	0.20	0.13
QNSE	1.2	1.8	1.7	1.2	0.13	0.25	0.19	0.15
YSU	1.5	2.2	2.0	1.5	0.16	0.31	0.21	0.19

characterized by a lower bias for wind speed, with the MYNN-UCM case having the best observations-model agreement.

Fig. 11S and Fig. 12S show the wind intensity differences between BL and MYJ bulk schemes and their corresponding BEP experiments. It is evident that higher negative values occur in correspondence of cells classified as urban. The effect of applying urban schemes is most evident in the MYJ wind speed difference map, with no substantial differences between daytime and nighttime. The differences between BL and BLBEP are less marked during the day, while they are appreciable at night.

As for the comparison with the observations, the time series of MYJBEP and BLBEP are the closest to the observations both for jet and synoptic days and at both the sites, due to the behavior described above. In particular, MYJBEP has an almost perfect agreement with observations at P24. It is also clear that YSU and ACM2 (solid lines in the figure) are the closest to observations among the bulk cases (i.e., with no urban scheme BEP) and QNSE and MYJ the most outlying. Also on breeze days schemes coupled with BEP perform better, especially at P24 during the night when the MBE is equal to 0.83 m/s and 0.44 m/s for BLBEP and MYJBEP (Table 10) and the MAE is equal to 0.99 m/s and 0.68 m/s (Table 11). QNSE and MYJ perform worse at P24 with nocturnal MBE just above 2 m/s. Although it is not easy to generalize the results for the two sites and the three regimes, our results are consistent with those of Avolio et al., 2017, who found that YSU and ACM2 schemes (with non-local closure) have the best performance among the PBL bulk schemes (Fig. 8).

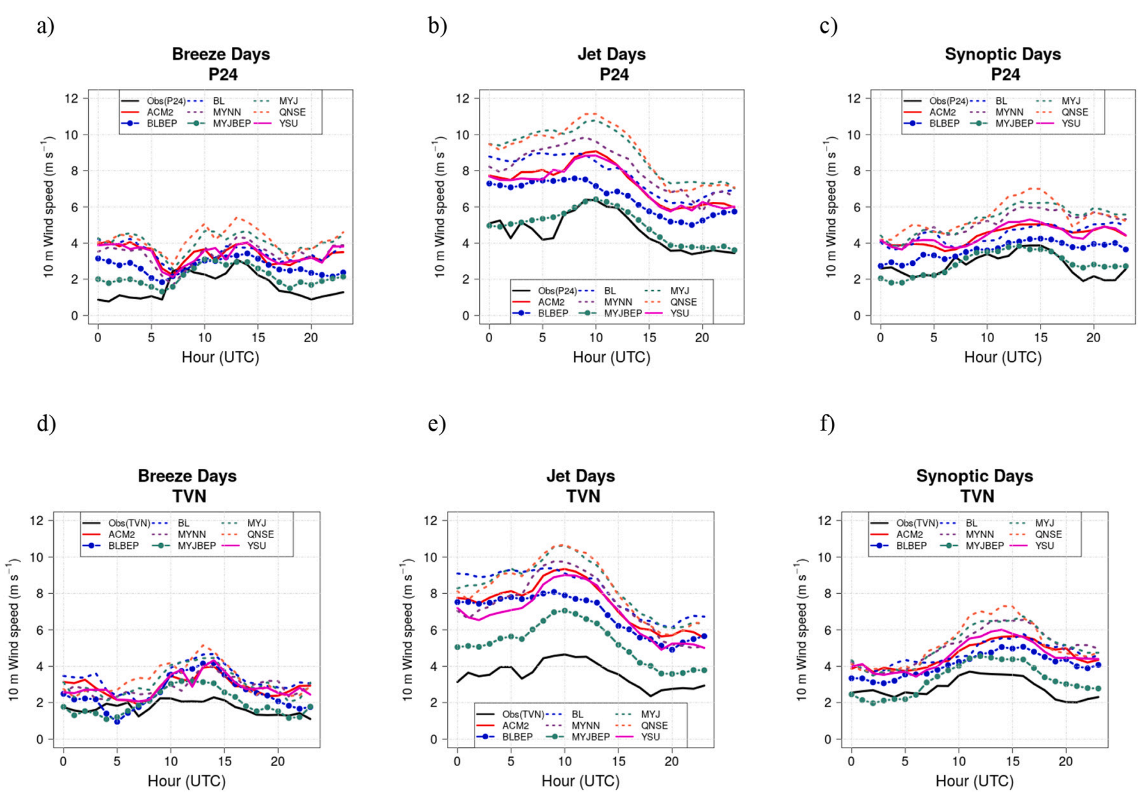

Fig. 8. Same as Fig. 4, but for 10 m wind speed.

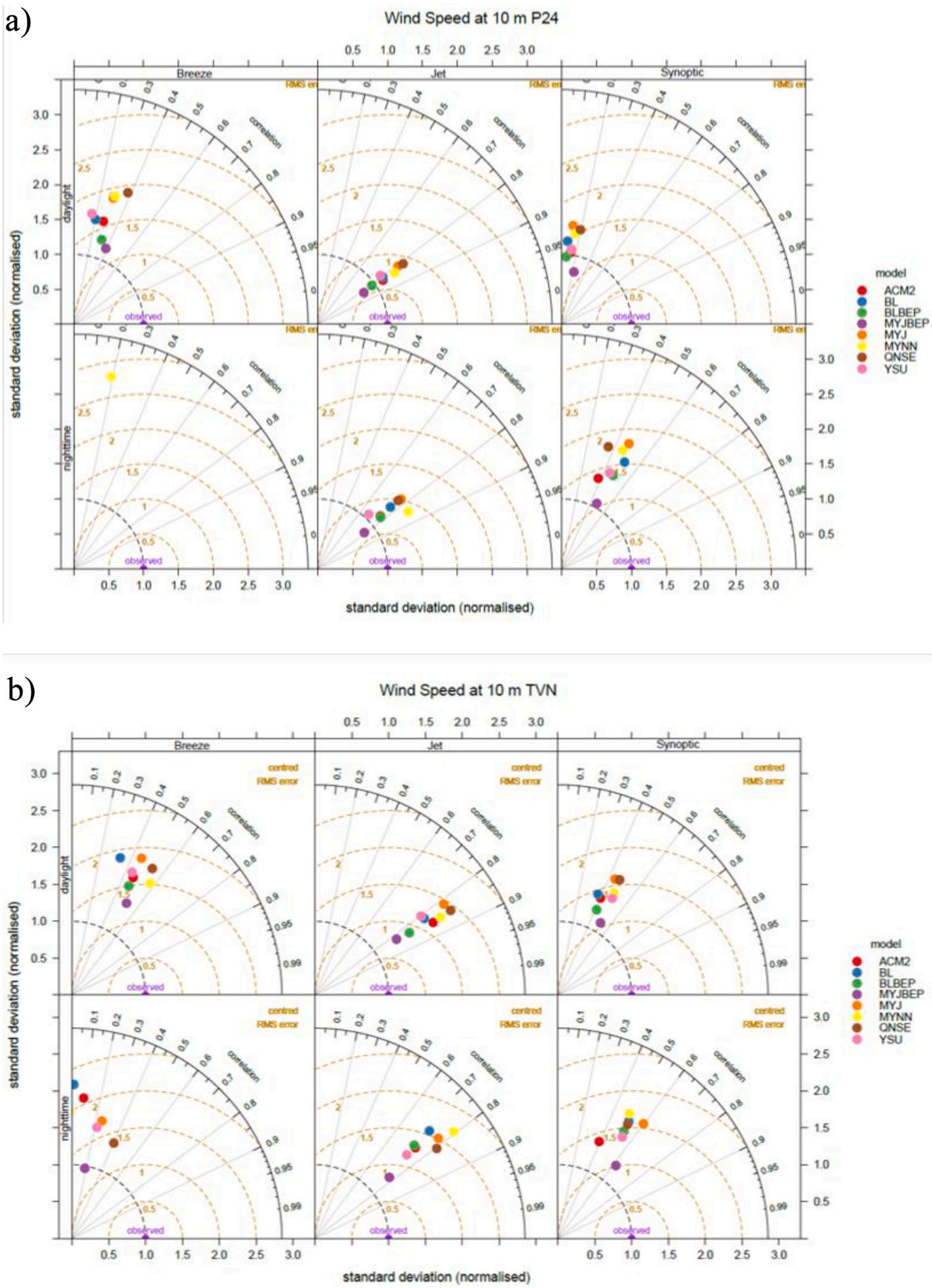

Fig. 9. Same as Fig. 7, but for 10 m wind speed.

Taylor diagrams in Fig. 9 show quite different R and NCRMSE values for the three regimes and the time slot, both at TVN and at P24. The breeze regime is characterized by a very poor correlation, with R between 0.5 and 0.2 during the day and lower than 0.1 or negative at night and with NCRMSE values higher than 2. This could be due to the fact that observed wind speed during breeze days is generally very low (<2 m/s) and it does not show a pronounced daily cycle. Jet days are characterized by a higher correlation, with R around 0.8 at P24 and between 0.7 and 0.8 at TVN. Also synoptic days display poor correlation, especially during the day with an R lower than 0.2 at P24, while during the night R does not exceed 0.5. Except for breeze days, NCRMSE are always lower than 2. In particular, on jet days NCRMSE is less than 1 for

Table 10
Mean Bias Error for wind speed at 10 m asl in (ms^{-1}).

Label	Breeze				Jet				Synoptic			
	P24		TVN		P24		TVN		P24		TVN	
	Day	Night	Day	Night	Day	Night	Day	Night	Day	Night	Day	Night
ACM2	0.59	1.8	1.0	1.3	2.2	2.7	4.1	3.4	1.6	2.3	1.8	1.8
BL	0.59	2.0	1.5	1.6	2.3	3.4	4.5	4.5	1.6	2.5	1.8	2.0
BLBEP	0.32	0.83	1.1	0.43	1.1	2.1	3.3	3.1	0.86	1.5	1.3	1.3
MYJBEP	−0.13	0.44	0.53	−0.011	0.11	0.17	2.0	1.2	0.33	0.30	0.69	0.13
MYJ	1.0	2.2	1.6	1.2	3.9	4.1	5.2	4.1	2.8	3.0	2.6	1.9
MYNN	0.74	2.1	1.1	1.3	3.2	3.3	4.5	2.8	2.4	2.8	2.5	2.0
QNSE	1.5	2.3	1.9	1.2	4.0	4.0	5.2	3.9	2.8	3.0	2.8	1.8
YSU	0.54	1.9	1.1	1.2	2.1	2.5	3.9	2.6	1.6	2.4	1.9	1.7

Table 11
Mean Absolute Error (MAE) and Normalized Mean Absolute Error (NMAE) for 10 m wind speed during breeze days.

Label	MAE				NMAE			
	P24		TVN		P24		TVN	
	Day	Night	Day	Night	Day	Night	Day	Night
ACM2	1.3	1.9	1.3	1.5	0.26	0.85	0.24	0.56
BL	1.5	2.0	1.8	1.8	0.30	0.89	0.32	0.68
BLBEP	1.2	0.99	1.5	1.2	0.22	0.45	0.26	0.47
MYJBEP	0.89	0.68	1.1	0.70	0.18	0.30	0.19	0.27
MYJ	1.6	2.2	1.8	1.3	0.32	1.00	0.31	0.51
MYNN	1.4	2.1	1.4	1.5	0.28	0.96	0.25	0.58
QNSE	1.8	2.3	2.0	1.2	0.36	1.03	0.35	0.47
YSU	1.3	2.0	1.4	1.3	0.27	0.90	0.25	0.50

all cases at P24. BEP coupled schemes present lower NCRMSEs than other schemes due to normalized standard deviations closer to one. This is especially pronounced for MYJBEP at TVN.

3.1.4. Wind speed direction

Fig. 10 exhibits the wind rose diagrams at P24. The results of some numerical cases are very similar to each other, therefore, to avoid redundancy, results of BL, BLBEP, MYJ and MYJBEP cases are shown in the main text, while results of MYNN (similar to those of BL), ACM2, QNSE and YSU cases (similar to those of MYJ) are presented in the supplementary material (Fig. 13S). The wind roses at TVN also are included and discussed in the supplementary material (Fig. 14S). The observations show that the prevalent wind direction during the measurement campaign is from south during daytime and south-east (SE) during night-time both at P24 and TVN. A more pronounced breeze dynamics and additional SE components during the jet days are detected at TVN. During breeze days, winds clearly rotate due to the local wind dynamic of coastal breeze, with winds from the sea during daytime and from land during night-time. Winds are prevalently from south/south-east when the synoptic conditions are superimposed onto the local dynamics.

Concerning P24 (Fig. 10), during the breeze daytime all the PBL schemes simulate a south-east component absent in the observations. The north-west component characterizing the breeze day is only partially visible in the BLBEP and MYJBEP cases. As for the night hours, all the PBL schemes (except MYJBEP) simulate a south/south-east component not present in the observations.

During the jet days the simulated wind directions have an east/southeast component, while in the observations the predominant component is from the South. During the night the simulations show a rotation of 35° clockwise with wind speeds overestimated by all PBL schemes except MYJBEP. In addition to the clockwise rotation, the BL, BLBEP and MYNN schemes also have a south/south-east component comparable to the small component from the south present in the observations.

As for the synoptic regime, the observations show a prevailing South and East-South direction during the day and night, respectively. The PBL BLBEP and MYJBEP schemes are able to faithfully reproduce the wind speeds. In terms of direction, the daytime South component is not markedly present, while the predominantly South-East direction is reproduced at night together with a North-East component absent in the observations. The YSU, ACM2, BL and MYNN schemes show wind directions comparable to observations especially at night.

3.2. Temperature and wind speed at 120 m height

At the TVN site, temperature and wind speed data at 120 m height were also recorded (See Fig. 11). At this height, the modeled daily cycles of temperature are quite close to each other, with the exception of the MYNN case. Indeed, the MYNN case differs from the other cases due to colder simulated values, especially under the jet regime. As already discussed about 2 m temperature, this could be due to the wind that is stronger than at the surface also during breeze and synoptic days. Corresponding MAE and the NMAE assume much higher values than in the other cases, both during daytime and nighttime (Table 13 and Table 14). The NMAE for MYNN is higher than twice the NMAE for BLBEP on jet days. Breeze days and nights are not characterized by such significant difference between MAE and NMAE of MYNN and the other experiments.

Regarding the comparison with the observations, daytime MBE is cold (negative) for the three regimes and for almost all cases like for 2 m temperature (Table 12). Only in the synoptic regime four cases (i.e., ACM2, BL, BLBEP, YSU) overestimate the temperature, with consequent positive MBE. BL and BLBEP cases are characterized by very low daytime MBE during breeze and synoptic days. The average daily cycle of the MYNN case, as observed above, significantly underestimates the temperature throughout jet days, therefore the MBE and MAE have very close absolute values both at night and daylight. Such values are not exactly the same since the non-averaged time series of the simulated temperature occasionally overestimates the observations.

The Taylor plot in Fig. 12a shows that NCRMSE is between 1 and 0.5 for all the experiments (except for QNSE during synoptic nights). On the other side, the correlation coefficient varies with the PBL scheme for each regime between 0.5 and 0.85. On synoptic days the normalized standard deviation is very close to 1 for all the numerical experiments, which are also equal in terms of R ($R = 0.8$) and NCRMSE (just above 0.5) during the daylight. An excellent WRF-observation agreement is confirmed (except for the MYNN case) by MBE values even lower than 0.1 °C, MAE around 0.8 °C and NMAE lower than 10% of the observed values (Table 12, Table 13, Table 14). The inclusion of the BEP urban scheme does not significantly affect the results even in the evening or at night, contrary to what happens at the surface.

The wind speed intensity observed at 120 m is approximately twice as much as at 10 m for all three regimes. It is worth noting that all cases overestimate observations, consequently all MBE values are positive in Table 12). During the breeze and synoptic regimes results of the numerical experiments are very close to each other. In particular, during

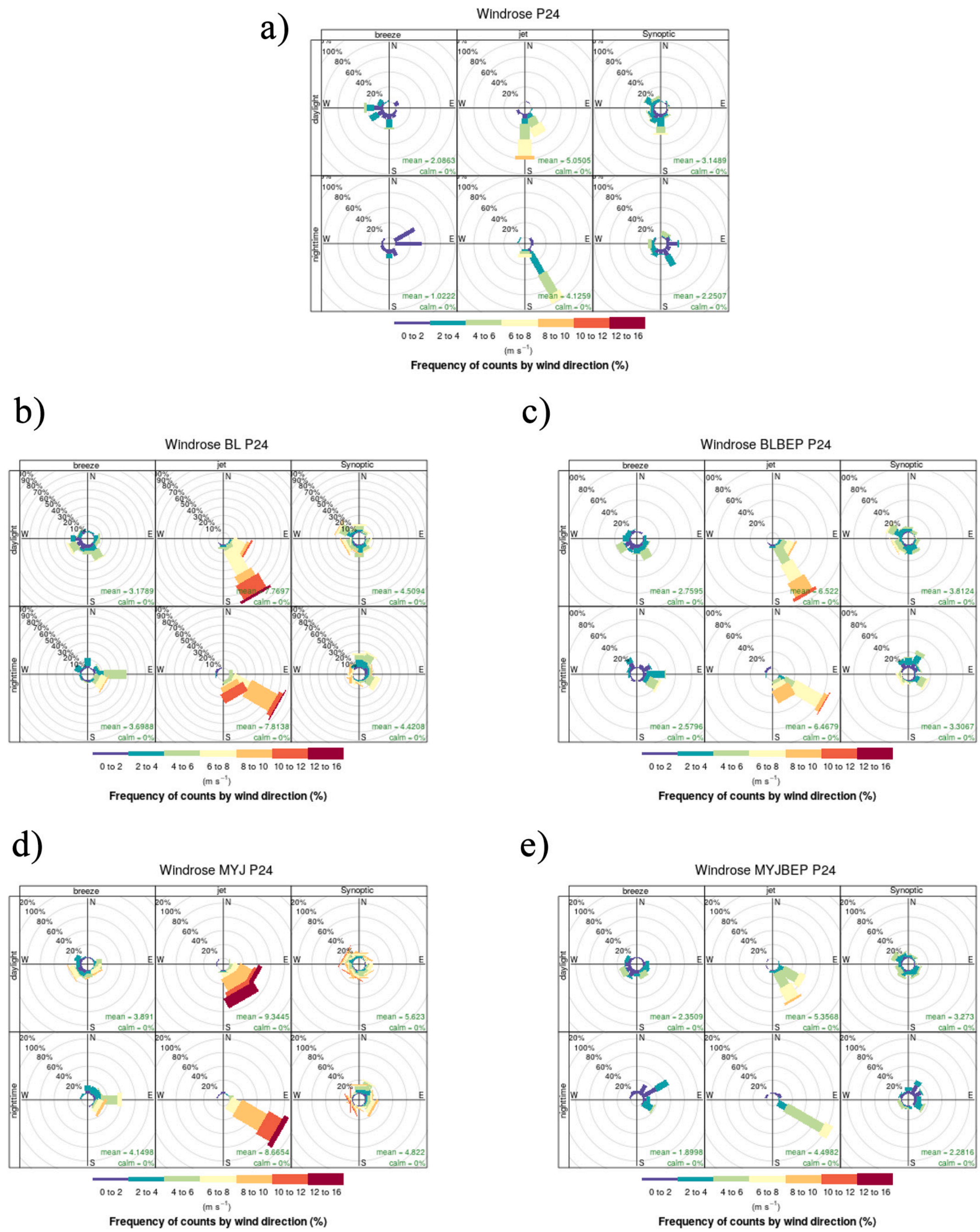

Fig. 10. Wind roses for the observations (a) and for the numerical experiments (b-g) at the P24 site.

the synoptic nights and the early mornings the curves are essentially overlapping and the markers in the Taylor diagram are quite close. During the jet regime, WRF particularly overestimate observations (MAEs are higher than other regimes for each case) and the curves of the different numerical experiments are much better distinguishable: ACM2 and YSU data are comparable and likewise MYJBEP and QNSE, while the urban BEP scheme improves the agreement of the BL scheme with the observations. In the Taylor plot the ACM2 and YSU markers are very close, with R equal to 0.8 and 0.7 during the daylight and nighttime respectively. Furthermore, the normalized standard deviation is slightly higher during daytime and the normalized CRMSE is between 0.6 and 0.7.

BL has lower errors (MBE, MAE, NMAE) compared to the other schemes, with the exception of the BLBEP. For example, it has MBE equal to 3.7 m/s at night, while it is equal to 5.3 m/s for MYJ and MYJBEP. The MYJBEP has one of the worst performances, with the MAE equal to 3.8 m/s (daytime) and 5.4 m/s (nighttime) and the NMAE equal to 0.28 (daytime) and 0.42 (nighttime), while it exhibit the best agreement with the observations near the surface.

4. Conclusions

In this study we performed eight numerical experiments with the WRF model (~1 km of horizontal resolution) and compared the results to observations in order to investigate the effect of the PBL configuration on the simulation of near-surface weather variables in a coastal, port-industrial site with complex terrain. To this end, we applied six different surface layer-PBL scheme combinations, including two non-local (ACM2 and YSU) and four local (BL, MYJ, MYNN and QNSE) PBL schemes. We also considered the parameterization of the urban

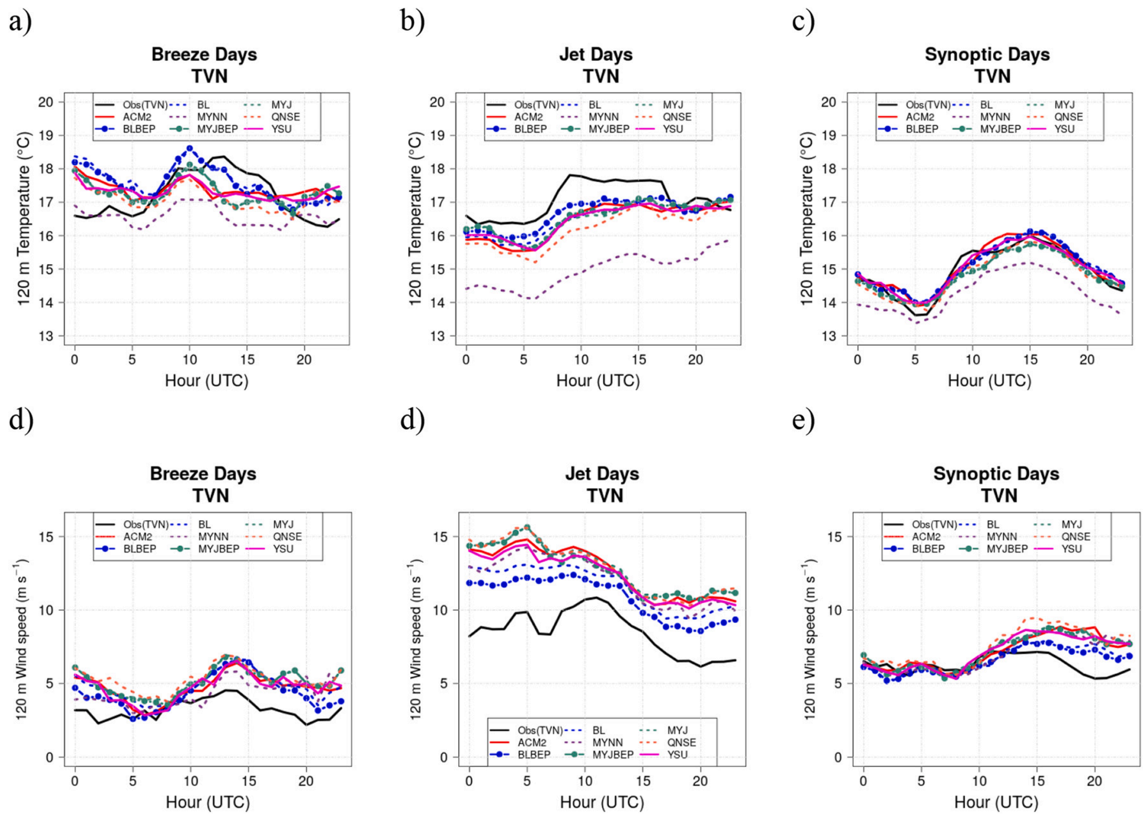

Fig. 11. Averaged daily time series of temperature (first row) and wind speed (second row) at 120 m height at TVN.

Table 12
Mean Bias Error (MBE) for the temperature and wind speed at 120 m during breeze, jet and synoptic regimes.

	Temperature						Wind speed					
Label	Breeze		Jet		Other		Breeze		Jet		Other	
	D	N	D	N	D	N	D	N	D	N	D	N
ACM2	−0.39	0.93	−0.80	−0.41	0.11	0.13	1.1	2.0	3.5	4.9	0.74	1.0
BL	−0.049	1.0	−0.67	−0.34	0.070	0.21	1.3	1.8	2.6	3.7	0.29	0.49
BLBEP	−0.089	0.93	−0.53	−0.23	0.098	0.14	1.2	1.1	2.0	2.7	0.16	0.33
MYJBEP	−0.45	0.81	−0.76	−0.24	−0.17	−0.029	1.5	2.3	3.4	5.3	0.79	1.0
MYJ	−0.45	0.85	−0.81	−0.22	−0.17	0.0051	1.6	2.3	3.7	5.3	0.91	1.0
MYNN	−1.1	0.055	−2.4	−1.7	−0.66	−0.65	0.67	1.6	3.2	4.1	0.50	0.9
QNSE	−0.67	0.66	−1.1	−0.59	−0.13	−0.057	1.7	2.5	3.6	5.3	1.2	1.3
YSU	−0.42	0.85	−0.83	−0.34	0.029	0.13	1.1	2.0	3.2	4.6	0.81	0.93

surface by coupling two of them (BL, MYJ) with the BEP scheme. Numerical results were evaluated against the data collected during a measurements campaign carried out in April 2016 at two sites on the Tyrrhenian coast (central Italy). Observed and simulated data were grouped on the basis of the atmospheric regime (breeze, jet, synoptic) and averaged for the illustration of the daily cycles and for the computation of the statistical metrics. A generalization of the results is challenging since both the model-to-observation and the intra-model comparisons vary with location (P24 or TVN), meteorological variable (temperature, wind speed, wind direction, solar radiation), measurement level (near-surface or 120 m MSL) and with the circulation regime (breeze, jet, synoptic).

The thermal field simulated by the local schemes (BL, MYJ, MYNN, QNSE) do not differ markedly in terms of magnitude from those of the non-local schemes (ACM2, YSU), with ACM2 and BL being the hottest and QNSE and MYNN the coldest. The time series of non-local schemes are much closer to each other than those of local schemes. MYNN significantly underestimates the observations, deviating from the other schemes. This suggests that the choice of the PBL parameterization is not the main driver of the temperature model bias, which could possibly be associated with a poor representation of the local surface-atmosphere energy exchange. Indeed, the application of the urban BEP scheme has an important impact when combined with BL, especially in the evening and at night. It greatly improves the model-observation agreement both at TVN and P24 during jet days, while it impairs the agreement during the "breeze" days. During jet nights, MBEs changes from −1.3 °C of BL to −0.93 °C of BLBEP at P24 and from −0.39 °C to 0.076 °C at TVN. In contrast, during breeze nights, MBE changes from 0.89 °C of BL to 2.2 °C of BLBEP at P24 and from 0.97 °C of BL to 1.9 °C of BLBEP at TVN. The non-local PBL schemes have very similar skills in simulating 10 m wind speed, while local PBL schemes (especially MYNN) differ more among each other. The model reproduces well the daily wind cycle at 10 m, even if it shows a substantial overestimation, especially nighttime. The benefit of the introduction of the urban BEP scheme in terms of bias is evident, with a significant reduction of the MBE (e.g., from 2 °C to 0.83 °C for BL and BLBEP at P24 and from 1.2 °C to −0.011 °C at TVN during breeze nights). This points out again the key role of the surface-atmosphere interface. BEP coupled schemes present lower NCRMSEs

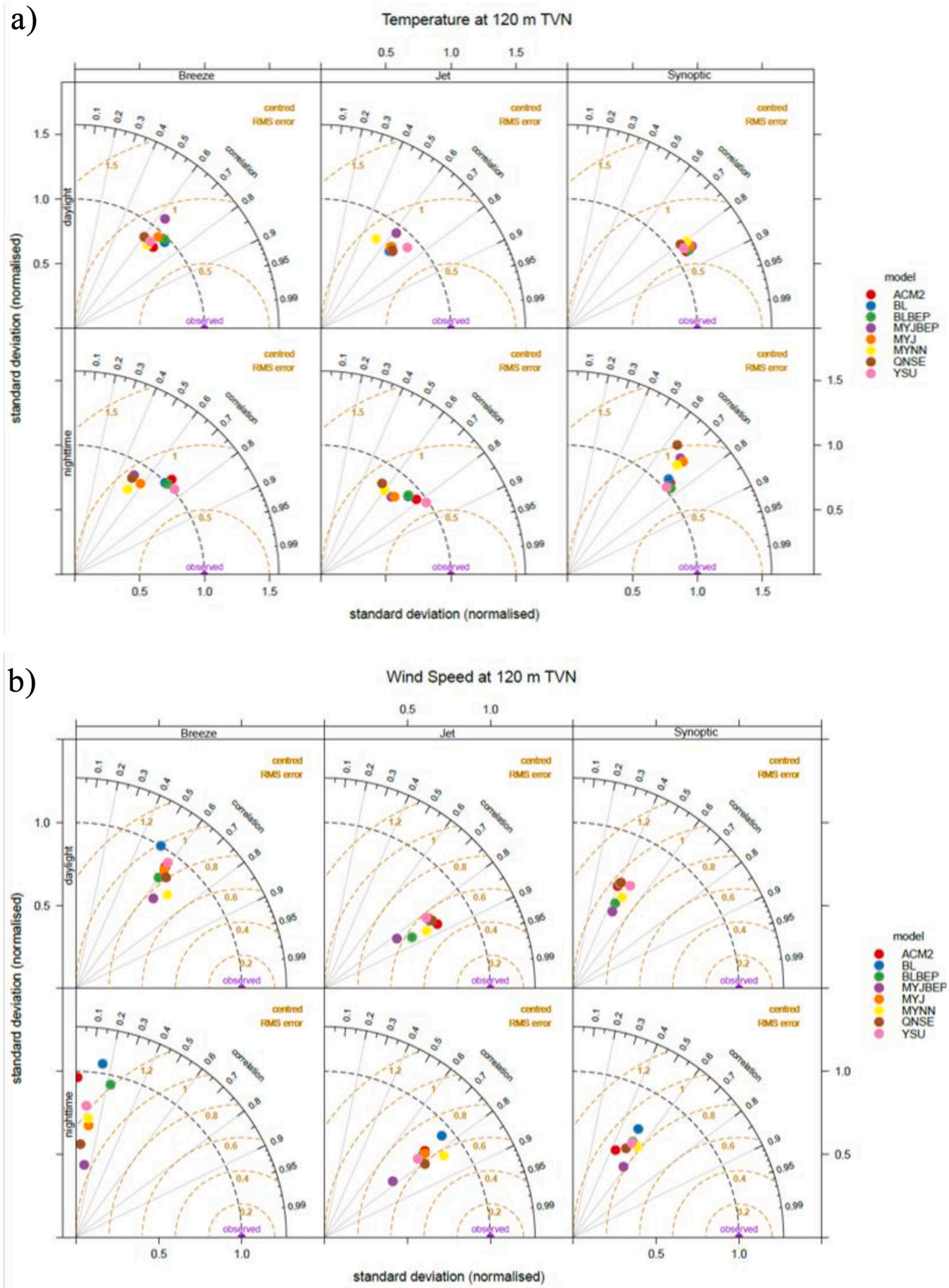

Fig. 12. Taylor diagrams for temperature (a) and wind speed (b) at 120 m height at TVN.

than other schemes due to normalized standard deviations closer to one. This is especially pronounced for MYJBEP at TVN. The BLBEP confirms excellent performances even at 120 m, unlike MJYBEP which has one of the highest MBEs. Indeed, daytime MBE is equal to 2 m/s and 0.16 m/s during the jet and the synoptic regime respectively for the BLBEP case and 3.4 m/s and 0.79 m/s for the MYJBEP case. Corresponding nighttime values of MBE are equal to 2.7 m/s (jet) and 0.33 m/s (synoptic) for BLBEP case and equal to 5.3 m/s (jet) and 1.0 m/s (synoptic) for MYJBEP.

Although local and non-local PBL schemes are considered more accurate in simulating near-surface variables in stable and unstable conditions respectively, our results do not show a large dissimilarity in the performances of the two classes of schemes between daytime and nighttime, probably due to the peculiarities of the sites (complexity of

Table 13
Mean Absolute Error (MAE) for the temperature and wind speed at 120 m during breeze, jet and synoptic regimes.

Label	Temperature						Wind speed					
	Breeze		Jet		Other		Breeze		Jet		Other	
	D	N	D	N	D	N	D	N	D	N	D	N
ACM2	1.6	1.5	1.2	0.76	0.79	0.89	2.2	2.7	3.9	4.9	2.6	3.1
BL	1.5	1.5	1.1	0.77	0.81	0.78	2.2	2.4	3.0	3.8	2.3	3.0
BLBEP	1.5	1.4	1.1	0.70	0.78	0.79	2.1	2.0	2.5	3.1	2.3	2.7
MYJBEP	1.5	1.4	1.2	0.74	0.82	0.83	2.3	3.1	3.8	5.4	2.6	2.8
MYJ	1.5	1.4	1.2	0.74	0.83	0.84	2.4	3.1	4.0	5.4	2.7	2.8
MYNN	1.7	1.1	2.4	1.83	1.09	1.16	1.9	2.6	3.5	4.5	2.6	2.9
QNSE	1.6	1.3	1.3	0.88	0.79	0.95	2.3	3.0	3.8	5.5	2.8	3.1
YSU	1.4	1.3	1.1	0.69	0.79	0.81	2.2	2.8	3.7	4.7	2.5	2.9

Table 14
Normalized Mean Absolute Error (NMAE) for the temperature and wind speed at 120 m during breeze, jet and synoptic regimes.

Label	Temperature						Wind speed					
	Breeze		Jet		Other		Breeze		Jet		Other	
	D	N	D	N	D	N	D	N	D	N	D	N
ACM2	0.17	0.19	0.17	0.13	0.068	0.097	0.20	0.46	0.29	0.38	0.19	0.24
BL	0.17	0.19	0.17	0.13	0.069	0.084	0.21	0.42	0.22	0.29	0.17	0.23
BLBEP	0.17	0.18	0.16	0.12	0.066	0.085	0.19	0.34	0.19	0.24	0.17	0.21
MYJBEP	0.17	0.18	0.18	0.12	0.070	0.090	0.21	0.52	0.28	0.42	0.19	0.21
MYJ	0.16	0.18	0.18	0.12	0.071	0.091	0.22	0.53	0.30	0.42	0.19	0.21
MYNN	0.19	0.15	0.36	0.30	0.093	0.13	0.18	0.45	0.26	0.35	0.19	0.22
QNSE	0.18	0.17	0.20	0.14	0.067	0.103	0.21	0.51	0.28	0.43	0.20	0.24
YSU	0.15	0.17	0.17	0.11	0.067	0.087	0.20	0.47	0.27	0.37	0.18	0.23

orography and local circulations in the area) and of the different surface layer schemes applied (Shin and Hong, 2011).

Concerning the wind direction, the main differences are noted during the jet days, when a strong South/South-East component of the wind prevails: all the model configurations show a counterclockwise deviation of about 30°, which is possibly associated with a misrepresentation of the local topography in the global analysis.

The simulation of the incident solar radiation is not significantly influenced by the configuration used as all the PBL schemes provide very similar values, except for MYNN on jet and synoptic days as for the temperature at 2 m.

Based on the tests carried out here, we plan for future work a better characterization and analysis of the surface-atmosphere exchange, preferentially focusing on the following topics: i) detailed measurements of the energy fluxes and ii) micrometeorological parameters (Ciardini et al., 2019; Sozzi et al., 2020), iii) clarification of the role of global boundary conditions on the simulation in the nested domains.

Declaration of Competing Interest

The authors declare that they have no known competing financial interests or personal relationships that could have appeared to influence the work reported in this paper.

Acknowledgements

The computational resources for WRF runs were provided by the Gran Sasso National Laboratories (LNGS) in the framework of project ARIAPROBA. We acknowledge the LNGS for the availability of high-performance computing resources and support, and ENEL for providing the sonic anemometer measurements in the framework of a convention with CNR-ISAC. The April 2016 intensive measurement campaign was performed in the framework of the AIRSEALAB project funded by CNR and made possible thanks to the support of the Rome Ports Authority.

Ilaria Gandolfi gratefully acknowledges support by the PON-AIM project 1858058-3-SSD-FIS/06. Serena Falasca was founded by the project RAFAEL code ARS01_00305 - PON R&I 2014-2020 and the project RHAPS code 2017MSN7M8 - PRIN 2017, both from the Italian Ministry University and Research (MUR).

Appendix A. Supplementary data

Supplementary data to this article can be found online at https://doi.org/10.1016/j.atmosres.2021.105824.

References

Angevine, W.M., Jiang, H., Mauritsen, T., 2010. Performance of an eddy diffusivity–mass flux scheme for shallow cumulus boundary layers. Mon. Weather Rev. 138, 2895–2912. https://doi.org/10.1175/2010MWR3142.1.

Arrillaga, J.A., Yagüe, C., Sastre, M., Román-Cascón, C., 2016. A characterisation of sea-breeze events in the eastern Cantabrian coast (Spain) from observational data and WRF simulations. Atm. Res. 181, 265–280. https://doi.org/10.1016/j.atmosres.2016.06.021.

Avolio, E., Federico, S., Miglietta, M.M., Lo Feudo, T., Calidonna, C.R., Sempreviva, A.M., 2017. Sensitivity analysis of WRF model PBL schemes in simulating boundary-layer variables in southern Italy: an experimental campaign. Atmos. Res. 192, 58–71. https://doi.org/10.1016/j.atmosres.2017.04.003.

Banks, R.F., Baldasano, J.M., 2016. Impact of WRF model PBL schemes on air quality simulations over Catalonia, Spain. Sci. Total Environ. 572, 98–113. https://doi.org/10.1016/j.scitotenv.2016.07.167.

Banks, R.F., Tiana-Alsina, J., Baldasano, J.M., Rocadenbosch, F., Papayannis, A., Solomos, S., Tzanis, C.G., 2016. Sensitivity of boundary-layer variables to PBL schemes in the WRF model based on surface meteorological observations, lidar, and radiosondes during the HygrA-CD campaign. Atmos. Res. 176–177, 185–201. https://doi.org/10.1016/j.atmosres.2016.02.024.

Bonner, W.D., 1968. Climatology of the low level jet. Mon. Weather Rev. 96, 833–850. https://doi.org/10.1175/1520-0493(1968)096<0833:COTLLJ>2.0.CO;2.

Bougeault, P., LaCarrere, P., 1989. Parameterization of orography-induced turbulence in a mesobeta-scale model. Mon. Wea. Rev. 117, 1872–1890. https://doi.org/10.1175/1520-0493(1989)117<1872:POOITI>2.0.CO;2.

Bretherton, C.S., Park, S., 2009. A new moist turbulence parameterization in the Community Atmosphere Model. J. Clim. 22, 3422–3448. https://doi.org/10.1175/2008JCLI2556.1.

Carslaw, D.C., 2015. The openair manual — open-source tools for analyzing air pollution data. Manual for version 1.1-4. King's College London.

Carslaw, D.C., Ropkins, K., 2012. Openair — an R package for air quality data analysis. Environ. Model Softw. 27–28, 52–61. https://doi.org/10.1016/j.envsoft.2011.09.008.

Chaouch, N., Temimi, M., Weston, M., Ghedira, H., 2017. Sensitivity of the meteorological model WRF-ARW to planetary boundary layer schemes during fog conditions in a coastal arid region. Atmos. Res. 187, 106–127. https://doi.org/10.1016/j.atmosres.2016.12.009.
Ciancio, V., Falasca, S., Golasi, I., Curci, G., Coppi, M., Salata, F., 2018. Influence of input climatic data on simulations of annual energy needs of a building: energyplus and WRF modeling for a case study in Rome (Italy). Energies 11, 2835. https://doi.org/10.3390/en11102835.
Ciardini, V., Caporaso, L., Sozzi, R., Petenko, I., Bolignano, A., Morelli, M., Melas, D., Argentini, S., 2019. Interconnections of the urban heat island with the spatial and temporal micrometeorological variability in Rome. Urban Clim. 29, 100493. https://doi.org/10.1016/j.uclim.2019.100493.
Cohen, A.E., Cavallo, S.M., Coniglio, M.C., Brooks, H.E., 2015. A review of planetary boundary layer parameterization schemes and their sensitivity in simulating southeastern U.S. cold season severe weather environments. Weather Forecast. 30, 591–612. https://doi.org/10.1175/WAF-D-14-00105.1.
de la Paz, D., Borge, R., Martilli, A., 2016. Assessment of a high resolution annual WRF-BEP/CMAQ simulation for the urban area of Madrid (Spain). Atmos. Environ. 144, 282–296. https://doi.org/10.1016/j.atmosenv.2016.08.082.
Emery, C., Liu, Z., Russell, A.G., Odman, M.T., Yarwood, G., Kumar, N., 2017. Recommendations on statistics and benchmarks to assess photochemical model performance. J. Air Waste Manage. Assoc. 67, 582–598. https://doi.org/10.1080/10962247.2016.1265027.
Falasca, S., Curci, G., 2018. High-resolution air quality modeling: sensitivity tests to horizontal resolution and urban canopy with WRF-CHIMERE. Atmos. Environ. 187, 241–254. https://doi.org/10.1016/j.atmosenv.2018.05.048.
Falasca, S., Curci, G., Salata, F., 2021. On the association between high outdoor thermo-hygrometric comfort index and severe ground-level ozone: a first investigation. Environ. Res. 195, 110306. https://doi.org/10.1016/j.envres.2020.110306.
Feng, S., Lauvaux, T., Newman, S., Rao, P., Ahmadov, R., Deng, A., Díaz-Isaac, L.I., Duren, R.M., Fischer, M.L., Gerbig, C., Gurney, K.R., Huang, J., Jeong, S., Li, Z., Miller, C.E., O'Keeffe, D., Patarasuk, R., Sander, S.P., Song, Y., Wong, K.W., Yung, Y. L., 2016. Los Angeles megacity: a high-resolution land–atmosphere modelling system for urban CO_2 emissions. Atmos. Chem. Phys. 16, 9019–9045. https://doi.org/10.5194/acp-16-9019-2016.
Ferrero, E., Alessandrini, S., Vandenberghe, F., 2018. Assessment of planetary-boundary-layer schemes in the weather research and forecasting model within and above an urban canopy layer. Boundary-Layer Meteorol 168, 289–319. https://doi.org/10.1007/s10546-018-0349-3.
Ferretti, R., Mastrantonio, G., Argentini, S., Santoleri, R., Viola, A., 2003. A model-aided investigation of winter thermally driven circulation on the Italian Tyrrhenian coast: A case study: model-aided study of winter thermally driven circulation. J. Geophys. Res. 108 https://doi.org/10.1029/2003JD003424.
Garratt, J.R., Physick, W.L., 1985. The inland boundary layer at low latitudes: II Sea-breeze influences. Boundary-Layer Meteorol 33, 209–231. https://doi.org/10.1007/BF00052056.
Giannaros, T.M., Melas, D., Daglis, I.A., Keramitsoglou, I., Kourtidis, K., 2013. Numerical study of the urban heat island over Athens (Greece) with the WRF model. Atmos. Environ. 73, 103–111. https://doi.org/10.1016/j.atmosenv.2013.02.055.
Gioli, B., Gualtieri, G., Busillo, C., Calastrini, F., Gozzini, B., Miglietta, F., 2014. Aircraft wind measurements to assess a coupled WRF-CALMET mesoscale system: Atmospheric models are assessed against aircraft wind measurements. Met. Apps 21, 117–128. https://doi.org/10.1002/met.1419.
Gobbi, G.P., Di Liberto, L., Barnaba, F., 2020. Impact of port emissions on EU-regulated and non-regulated air quality indicators: the case of Civitavecchia (Italy). Sci. Total Environ. 719, 134984. https://doi.org/10.1016/j.scitotenv.2019.134984.
Grenier, H., Bretherton, C.S., 2001. A moist PBL parameterization for large-scale models and its application to subtropical cloud-topped marine boundary layers. Mon. Weather Rev. 129, 357–377. https://doi.org/10.1175/1520-0493(2001)129<0357:AMPPFL>2.0.CO;2.
Gunwani, P., Mohan, M., 2017. Sensitivity of WRF model estimates to various PBL parameterizations in different climatic zones over India. Atmos. Res. 194, 43–65. https://doi.org/10.1016/j.atmosres.2017.04.026.
Gunwani, P., Sati, A.P., Mohan, M., Gupta, M., 2020. Assessment of physical parameterization schemes in WRF over national capital region of India. Meteorog. Atmos. Phys. https://doi.org/10.1007/s00703-020-00757-y.
Hasan, M.A., Islam, A.K.M.S., 2018. Evaluation of microphysics and cumulus schemes of WRF for forecasting of heavy monsoon rainfall over the southeastern hilly region of Bangladesh. Pure Appl. Geophys. 175, 4537–4566. https://doi.org/10.1007/s00024-018-1876-z.
Hodges, D., Pu, Z., 2019. Characteristics and variations of low-level jets and environmental factors associated with summer precipitation extremes over the great plains. J. Clim. 32, 5123–5144. https://doi.org/10.1175/JCLI-D-18-0553.1.
Hong, S.-Y., Noh, Y., Dudhia, J., 2006. A new vertical diffusion package with an explicit treatment of entrainment processes. Mon. Weather Rev. 134, 2318–2341. https://doi.org/10.1175/MWR3199.1.
Janjic, Z.I., 1994. The step-mountain Eta coordinate model: further developments of the convection, viscous layer, and turbulence closure schemes. Mon. Wea. Rev. 122, 927–945.
Jeworrek, J., West, G., Stull, R., 2019. Evaluation of cumulus and microphysics parameterizations in WRF across the convective gray zone. Weather Forecast. 34, 1097–1115. https://doi.org/10.1175/WAF-D-18-0178.1.
Jia, W., Zhang, X., 2020. The role of the planetary boundary layer parameterization schemes on the meteorological and aerosol pollution simulations: a review. Atmos. Res. 239, 104890. https://doi.org/10.1016/j.atmosres.2020.104890.
Jiménez, P.A., Dudhia, J., 2012. Improving the representation of resolved and unresolved topographic effects on surface wind in the WRF model. J. Appl. Meteorol. Climatol. 51, 300–316. https://doi.org/10.1175/JAMC-D-11-084.1.
Karki, R., Hasson, S. ul, Gerlitz, L., Talchabhadel, R., Schenk, E., Schickhoff, U., Scholten, T., Böhner, J., 2018. WRF-based simulation of an extreme precipitation event over the Central Himalayas: atmospheric mechanisms and their representation by microphysics parameterization schemes. Atmos. Res. 214, 21–35. https://doi.org/10.1016/j.atmosres.2018.07.016.
Kuik, F., Lauer, A., Churkina, G., Denier van der Gon, H.A.C., Fenner, D., Mar, K.A., Butler, T.M., 2016. Air quality modelling in the Berlin-Brandenburg region using WRF-Chem v3.7.1: sensitivity to resolution of model grid and input data (preprint). Atmos. Sci. https://doi.org/10.5194/gmd-2016-190.
Li, H., Zhou, Y., Wang, X., Zhou, X., Zhang, H., Sodoudi, S., 2019. Quantifying urban heat island intensity and its physical mechanism using WRF/UCM. Sci. Total Environ. 650, 3110–3119. https://doi.org/10.1016/j.scitotenv.2018.10.025.
Perpinan Lamigueiro, O.: tdr: Target Diagram, available at: https://cran.r-project.org/package=tdr (last access: 10 January 2018), 2015.
Martilli, A., Clappier, A., Rotach, M.W., 2002. An urban surface exchange parameterisation for mesoscale models. Bound.-Layer Meteorol. 104, 261–304. https://doi.org/10.1023/A:1016099921195.
Mastrangelo, D., Horvath, K., Riccio, A., Miglietta, M.M., 2011. Mechanisms for convection development in a long-lasting heavy precipitation event over southeastern Italy. Atmos. Res. 100, 586–602. https://doi.org/10.1016/j.atmosres.2010.10.010.
Matthias, V., Bewersdorff, I., Aulinger, A., Quante, M., 2010. The contribution of ship emissions to air pollution in the North Sea regions. Environ. Pollut. 158, 2241–2250. https://doi.org/10.1016/j.envpol.2010.02.013.
Nakanishi, M., Niino, H., 2006. An improved Mellor–Yamada level-3 model: its numerical stability and application to a regional prediction of advection fog. Boundary-Layer Meteorol 119, 397–407. https://doi.org/10.1007/s10546-005-9030-8.
Nakanishi, M., Niino, H., 2009. Development of an improved turbulence closure model for the atmospheric boundary layer. J. Meteor. Soc. Japan 87, 895–912.
Noh, Y., Cheon, W.G., Hong, S.-Y., Raasch, S., 2003. Improvement of the K-profile model for the planetary boundary layer based on large eddy simulation data. Bound.-Layer Meteorol. 107, 401.
Petenko, I., Mastrantonio, G., Viola, A., Argentini, S., Coniglio, L., Monti, P., Leuzzi, G., 2011. Local circulation diurnal patterns and their relationship with large-scale flows in a coastal area of the Tyrrhenian Sea. Boundary-Layer Meteorol 139, 353–366. https://doi.org/10.1007/s10546-010-9577-x.
Petenko, I., Casasanta, G., Bucci, S., Kallistratova, M., Sozzi, R., Argentini, S., 2020. Turbulence, low-level jets, and waves in the Tyrrhenian coastal zone as shown by Sodar. Atmosphere 11, 28. https://doi.org/10.3390/atmos11010028.
Pleim, J.E., 2007. A combined local and nonlocal closure model for the atmospheric boundary layer. Part I: model description and testing. J. Appl. Meteorol. Climatol. 46, 1383–1395. https://doi.org/10.1175/JAM2539.1.
Querol, X., Gangoiti, G., Mantilla, E., Alastuey, A., Minguillón, M.C., Amato, F., Reche, C., Viana, M., Moreno, T., Karanasiou, A., Rivas, I., Pérez, N., Ripoll, A., Brines, M., Ealo, M., Pandolfi, M., Lee, H.-K., Eun, H.-R., Park, Y.-H., Escudero, M., Beddows, D., Harrison, R.M., Bertrand, A., Marchand, N., Lyasota, A., Codina, B., Olid, M., Udina, M., Jiménez-Esteve, B., Soler, M.R., Alonso, L., Millán, M., Ahn, K.-H., 2017. Phenomenology of high-ozone episodes in NE Spain. Atmos. Chem. Phys. 17, 2817–2838. https://doi.org/10.5194/acp-17-2817-2017.
Reshmi Mohan, P., Srinivas, C.V., Yesubabu, V., Baskaran, R., Venkatraman, B., 2018. Simulation of a heavy rainfall event over Chennai in Southeast India using WRF: sensitivity to microphysics parameterization. Atmos. Res. 210, 83–99. https://doi.org/10.1016/j.atmosres.2018.04.005.
Ribeiro, F.N.D., Oliveira, A.P. de, Soares, J., Miranda, R.M. de, Barlage, M., Chen, F., 2018. Effect of sea breeze propagation on the urban boundary layer of the metropolitan region of Sao Paulo, Brazil. Atmos. Res. 214, 174–188. https://doi.org/10.1016/j.atmosres.2018.07.015.
Sathyanadh, A., Prabha, T.V., Balaji, B., Resmi, E.A., Karipot, A., 2017. Evaluation of WRF PBL parameterization schemes against direct observations during a dry event over the Ganges valley. Atmos. Res. 193, 125–141. https://doi.org/10.1016/j.atmosres.2017.02.016.
Shin, H.H., Hong, S.-Y., 2011. Intercomparison of planetary boundary-layer parametrizations in the WRF model for a single day from CASES-99. Boundary-Layer Meteorol 139, 261–281. https://doi.org/10.1007/s10546-010-9583-z.
Skamarock, W.C., Klemp, J.B., Dudhia, J., Gill, D.O., Liu, Z., Berner, J., Wang, W., Powers, J.G., Duda, M.G., Barker, D.M., Huang, X.-Y., 2019. A description of the advanced research WRF model version 4. Natl. Cent. Atmos. Res. Boulder, CO, USA 113.
Sozzi, R., Casasanta, G., Ciardini, V., Finardi, S., Petenko, I., Cecilia, A., Argentini, S., 2020. Surface and aerodynamic parameters estimation for urban and rural areas. Atmosphere 11, 147. https://doi.org/10.3390/atmos11020147.
Stull, Roland B., 1988. An introduction to boundary layer meteorology. Vol. 13. Springer Science & Business Media.
Stull, R.B., 2018. Practical Meteorology: An Algebra-Based Survey of Atmospheric Science. University of British Columbia, Vancouver, Canada.
Sukoriansky, S., Galperin, B., Perov, V., 2005. Application of a new spectral theory of stably stratified turbulence to the atmospheric boundary layer over sea ice. Boundary-Layer Meteorol 117, 231–257. https://doi.org/10.1007/s10546-004-6848-4.
Sun, B.-Y., Bi, X.-Q., 2019. Validation for a tropical belt version of WRF: sensitivity tests on radiation and cumulus convection parameterizations. Atmos. Oceanic Sci. Lett. 12, 192–200. https://doi.org/10.1080/16742834.2019.1590118.

Taylor, K.E., 2001. Summarizing multiple aspects of model performance in a single diagram. J. Geophys. Res. 106, 7183–7192. https://doi.org/10.1029/2000JD900719.

Teixeira, J.C., Fallmann, J., Carvalho, A.C., Rocha, A., 2019. Surface to boundary layer coupling in the urban area of Lisbon comparing different urban canopy models in WRF. Urban Clim. 28, 100454. https://doi.org/10.1016/j.uclim.2019.100454.

Thunis, P., Georgieva, E., Galmarini, S., 2011. A procedure for air quality models benchmarking. Prepared by the Joint Research Centre, Ispra, Italy (16 February 2011) http://fairmode.jrc.ec.europa.eu/document/fairmode/ WG1/WG2_SG4_benchmarking_V2.pdf.

Tomasi, E., Giovannini, L., Zardi, D., de Franceschi, M., 2017. Optimization of Noah and Noah_MP WRF land surface schemes in snow-melting conditions over complex terrain. Mon. Wea. Rev. 145, 4727–4745. https://doi.org/10.1175/MWR-D-16-0408.1.

Tyagi, B., Magliulo, V., Finardi, S., Gasbarra, D., Carlucci, P., Toscano, P., Zaldei, A., Riccio, A., Calori, G., D'Allura, A., Gioli, B., 2018. Performance analysis of planetary boundary layer parameterization schemes in WRF modeling set up over southern Italy. Atmosphere 9, 272. https://doi.org/10.3390/atmos9070272.

Xu, L., Liu, H., Du, Q., Xu, X., 2019. The assessment of the planetary boundary layer schemes in WRF over the central Tibetan Plateau. Atmos. Res. 230, 104644. https://doi.org/10.1016/j.atmosres.2019.104644.

Zemba, J., Friehe, C.A., 1987. The marine atmospheric boundary layer jet in the Coastal Ocean Dynamics Experiment. J. Geophys. Res. 92, 1489. https://doi.org/10.1029/JC092iC02p01489.

Zempila, M.-M., Giannaros, T.M., Bais, A., Melas, D., Kazantzidis, A., 2016. Evaluation of WRF shortwave radiation parameterizations in predicting Global Horizontal Irradiance in Greece. Renew. Energy 86, 831–840. https://doi.org/10.1016/j.renene.2015.08.057.

Zeng, X.-M., Wang, N., Wang, Y., Zheng, Y., Zhou, Z., Wang, G., Chen, C., Liu, H., 2015. WRF-simulated sensitivity to land surface schemes in short and medium ranges for a high-temperature event in East China: a comparative study: WRF sensitivity to land surface schemes. J. Adv. Model. Earth Syst. 7, 1305–1325. https://doi.org/10.1002/2015MS000440.

Zhang, Y., Yan, D., Wen, X., Li, D., Zheng, Z., Zhu, X., Wang, B., Wang, C., Wang, L., 2020. Comparative analysis of the meteorological elements simulated by different land surface process schemes in the WRF model in the Yellow River source region. Theor. Appl. Climatol. 139, 145–162. https://doi.org/10.1007/s00704-019-02955-0.